NASA
Technical
Paper
2254

April 1984

Test-Engine and Inlet Performance of an Aircraft Used for Investigating Flight Effects on Fan Noise

Robert A. Golub
and John S. Preisser

NASA

NASA
Technical
Paper
2254

1984

Test-Engine and Inlet Performance of an Aircraft Used for Investigating Flight Effects on Fan Noise

Robert A. Golub
and John S. Preisser

Langley Research Center
Hampton, Virginia

NASA
National Aeronautics
and Space Administration

Scientific and Technical
Information Branch

SUMMARY

As part of the NASA Flight Effects on Fan Noise Program, a Grumman OV-1B Mohawk aircraft was modified to carry a modified and instrumented Pratt & Whitney JT15D-1 turbofan engine. An instrumented research flight inlet, a fan-blade-mounted transducer instrumentation system, instrumentation for measuring aircraft state, and an onboard signal conditioning and recording system were developed and utilized to collect test-engine performance data and inlet source noise flight data. These onboard data, together with simultaneously measured far-field acoustic data, comprise a flight data base to which JT15D-1 static and wind-tunnel data can be compared. The overall objective is to improve the ability to use ground-based facilities for the prediction of flight inlet radiated noise. This report describes the hardware and presents performance results for the research engine.

INTRODUCTION

At the time of conception of the NASA Flight Effects on Fan Noise Program during the mid-1970's, it had become widely accepted throughout industry that there were significant shortcomings in the ability to predict inlet-generated aircraft flyover noise levels for turbofan engines on the basis of ground static engine tests (ref. 1). Previous attempts to reduce engine noise were successful because they did not require precise definition and understanding of how the noise source propagated from the engine.

The most prevalent noise-prediction theory during the mid-1970's was that of Tyler and Sofrin (ref. 2), which predicted a reduction in inlet-generated noise by judicious choices of the number and spacing between the rotor blades and stator vanes. However, it was also generally acknowledged that the predicted noise reductions were seldom achieved during ground static testing and that the tendency was for the ground test to overpredict the lower noise levels that would be measured during flight. During this period, it was thought that masking effects resulting from ingestion of ground and test structure generated vortices and from ingestion of near-ground atmospheric turbulence (different from that encountered during flight) were the cause of the higher noise levels measured in the ground static-test facilities (refs. 3 and 4). Also at about this same time, tests were performed which indicated that both inlet-geometry (ref. 5) and forward-velocity effects from the aircraft motion could significantly affect the noise source, radiation, and propagation.

More stringent noise certification requirements forced the development of finding the lowest cost-benefit mode of testing to achieve the required noise reduction. With many possible trade-offs for meeting specified in-flight noise goals, each noise-reduction technique would have to be evaluated against the potential penalties in weight, performance, and cost that it would impose on the aircraft and/or engine operation. To achieve an accurate prediction methodology, the proper identification of ground noise source levels, spectra, and directivity was necessary. Additionally, adjustments had to be made to static data to account for any atmospheric-propagation effects and forward-velocity effects. Another obvious requirement was the necessity to obtain an accurate flyover noise data base to validate the ground test data and adjustment procedures.

The NASA research program was initiated to provide the understanding and flight data base that would improve the ability to predict more accurately the inlet-generated flyover noise by using ground test facilities. It was designed to systematically identify and correlate ground static, wind-tunnel, and flyover measured noise (see fig. 1). The program was instituted by NASA between the Langley (LaRC), Lewis (LeRC), and Ames (ARC) Research Centers. LeRC assumed the responsibility for conducting outdoor static engine tests and fan tests in an anechoic chamber. The wind-tunnel tests were run in the Ames 40- by 80-Foot Wind Tunnel, which had been shown to yield good noise-measurement data for fan noise. LaRC measured the flight noise by using a test-bed aircraft to carry a test turbofan engine. A key element to the success of the program was to assure engine and hardware commonality among Centers and precise commonality of engine operating points throughout the matrix of test environments.

This paper addresses the commonality of program hardware, the LaRC flight tests, the test engine, and research inlet performance, and makes performance comparisons with data from the ground static tests and the wind-tunnel tests. Some program results on far-field acoustics, fan-blade fluctuating pressures, and stator-vane fluctuating pressures are contained in references 6 to 8.

Participation by industry and universities in the program was extensive. The workshop proceedings of reference 9 are an indication of the extent of their involvement.

SYMBOLS AND ABBREVIATIONS

BPF blade-passage frequency, Hz

c speed of sound, ft/sec

d duct diameter, in.

FPR fan pressure ratio

FM frequency modulation

g acceleration due to gravity, 32.2 ft/sec^2

ICD inlet control device

IRIG Inter-Range-Instrumentation Group

M mean inlet Mach number

M_{ac} Mach number of aircraft

M_t Mach number at fan-blade tip

$M_{t,rel}$ relative Mach number at fan-blade tip

N_1 fan speed, rpm

N_2 compressor speed, rpm

PCM pulse-code modulation

p_o standard atmospheric pressure at sea level, psi

p_s static pressure, psi

p_t total pressure, psi

R specific gas constant

RF radio frequency

T temperature, °F

T_o standard atmospheric temperature at sea level, °F

T_t total temperature, °F

V_∞ aircraft forward speed, knots

WB wideband

w inlet weight flow, lb/sec

x,y coordinates used to define inlet geometry (fig. 7)

α aircraft angle of attack, deg

$\alpha_{t,rel}$ relative incidence angle at fan-blade tip, deg

γ ratio of specific heats

δ pressure ratio, p_t/p_o

θ temperature ratio, T_t/T_o

θ_{em} emission angle at which far-field radiation pattern is measured (with respect to engine forward centerline axis), deg

ρ density of air, lb/ft^3

Subscripts:

bp bypass

corr corrected

f inlet at fan face

i inlet at station 30.000

A bar over a symbol indicates average value.

TEST VEHICLE AND ENGINE

Research Flight Technique

As mentioned in the preceding section, NASA LaRC obtained an accurate flyover-noise data base with which the ground static and wind-tunnel test data could be compared. This required the development of a highly sophisticated state-of-the-art, far-field, acoustic measurement technique and the development of a flying test-bed aircraft to accommodate the measurement technique and to safely achieve the program goals. A brief description of the research flight operation is given. More detailed descriptions are in reference 10, which describes a preliminary test run for "proof of concept" for the flight operations, and in reference 6, where a test with the JT15D-1 engine is described. Figure 2 is a schematic of the technique.

The flight measurement technique was based on state-of-the-art measurement technology which could yield narrow-band far-field spectra. The technique required an accurate determination of sound pressure level with a high resolution of the source location. Measurements of aircraft performance, test-engine performance, and source noise measurements were simultaneously recorded aboard the aircraft. All the recorded data were correlated using Inter-Range-Instrumentation Group (IRIG) A time code.

The far-field, acoustic measurement technique used a linear array of 10 microphones mounted atop 30-ft poles. These microphones were located on the runway, parallel to the centerline, to facilitate pilot ease of flying the aircraft over the array. The signals from the microphones were ensemble-averaged to yield the desired precision noise data. Details of the data-reduction computer program can be found in reference 11. The requirement for precision mandates that the aircraft location be known very accurately while it traverses the microphone array. Precision aircraft location was provided by the AN/FPS 16 (V) laser radar system at Wallops Flight Center (see ref. 12 for details). This system can determine the position of the aircraft to ±2 ft and, in conjunction with a minicomputer, can display the information in real time for use by the test director in the control tower (i.e., aircraft location with respect to the first pole microphone, aircraft sideline deviation, and aircraft altitude). Accurate far-field acoustic measurements taken under varying temperature and relative-humidity conditions require data corrections for propagation distances and weather conditions. Hence, detailed weather information was gathered by the use of a weather instrument package suspended beneath a tethered balloon positioned at the aircraft operating altitude. Weather data were recorded during each flyover. Between flyover measurements, ground-to-aircraft altitude weather profiles were recorded to preclude aircraft flyovers when weather anomalies existed.

The evolved-operations technique required the pilot to fly the aircraft in a racetrack pattern, traversing the microphones at a velocity of about 130 knots at an altitude of 300 ft. A particular flight test would consist of a series of aircraft test runs over the microphone array. The Pratt & Whitney JT15D-1 turbofan test-engine (the research-noise-source) fan speed was held constant during each particular run in a series, and was then changed for successive runs in a series.

Engine and Aircraft Selection

The JT15D-1 turbofan engine was selected as the test inlet noise source. Its small size made it attractive for static, wind-tunnel, and flight test research; NASA also had several of these engines readily available. Furthermore, some testing on measuring the static, wind-tunnel, and flight noise characteristics of a JT15D-1 engine had already been accomplished (refs. 13 to 15). Equally important, the construction of the JT15D-1 engine was similar to that of current larger turbofan engines, such as a Pratt & Whitney JT9D, for which static-to-flight noise comparisons have been made (ref. 16).

Once the JT15D-1 turbofan engine was selected, the aircraft selection became a task of identifying a test vehicle capable of carrying the test engine with minimum interference, that is, to provide the JT15D-1 engine with as clean an inflow as possible and with as few reflections as possible from other parts of the aircraft. An obvious choice was to use the JT15D-1 powered Cessna Citation aircraft, but its rear-fuselage-mounted engines ingest fuselage- and wing-induced vortices and the aircraft wings acoustically shield the engine inlets from forward view during approach and flyover (ref. 15).

A survey of available aircraft resulted in the selection of the Grumman OV-1B Mohawk. This two-place, twin turboprop is an electronic surveillance aircraft. (See table 1 for specifications.) It is extremely rugged, is designed to fly at slow speeds (80 to 250 knots) and to operate at low altitudes (<100 ft), and has excellent low-speed flight characteristics. It normally carries a pilot and an observer/surveillance-equipment operator.

Noise measurements of an OV-1B Mohawk turboprop engine (Lycoming T53-L-7) were compared with static noise data from the JT15D-1 engine. The background noise from the OV-1B test-bed aircraft was found to be sufficiently low, particularly in the range of frequencies where the fan blade-passage frequency tones would be present. Figure 3, which is actual flyover data taken during the flight research tests, shows a typical signal-to-noise ratio comparison for a JT15D-1 engine approach power setting of 10 800 rpm. The aircraft velocity was 130 knots, the altitude was approximately 300 ft, and the turboprop propeller turned at about 1600 rpm. At higher test-engine fan speeds, the JT15D-1 engine completely dominates at all frequencies in the spectra.

The manufacturer of the OV-1B Mohawk performed a "Feasibility Study for Installation and Test of a Pratt & Whitney Turbofan Engine (JT15D-1) on a Mohawk Aircraft" (ref. 17). The study included investigations of the JT15D-1 installation and its effects on aircraft aerodynamics, loads and dynamics, propulsion systems, and flight testing. Figure 4 is the aircraft/test-engine configuration which was determined to be optimal with respect to both the noise research mission and safety of flight.

Appendix A contains a more detailed description of the aircraft and engine modifications, as well as a detailed explanation of the operation and hardware layout of the JT15D-1 engine.

Installation Effects and Inlet Inflow Tests

During the course of the feasibility study, it was recognized that the selected aircraft/test-engine interface location could result in a configuration which had undesirable acoustic effects. Therefore, two separate series of flight tests were performed. The first test series consisted of flying a pure-tone acoustic source at the proposed test-engine location. (See ref. 10.) This series of flights was to determine whether there were any significant installation effects which could affect the acoustic radiation pattern or the measured far-field noise. The results indicated that, except for the very shallow angles (i.e., for propagation angles <20° measured from the horizon), no significant radiation pattern distortion existed. A range of aircraft speeds from 100 to 150 knots was investigated.

The second series of tests were executed to determine the extent of any inflow disturbances caused by the rotation of the turboprop propeller. The proposed JT15D-1 mounting position placed the tip of the propeller approximately 19 in. in front of the JT15D-1 engine-inlet plane and 25 in. from the centerline. (See fig. 4.) Five hot-film probes (fig. 5) were mounted on the OV-1B aircraft in place of the wing fuel tank. They were positioned in the plane of the proposed inlet plane of the test engine and were oriented along a line which passed through the centers of both engines. Probe A was located farthest from the propeller at a location corresponding to the inlet lip farthest from the propeller tip; probe B was located at the position corresponding to the test-engine centerline; probe C-D (cross-film probe) was located at the point of the inlet lip closest to the propeller tip; and probe E was located between the inlet and the propeller tip.

Shown below the photographs in figure 5 are typical results from one of the flight tests. These results show comparisons of the time histories of the fluctuating velocity fields as measured by each probe. To the left are the time histories measured by the probes while the number-2 turboprop engine was operated at 1600 rpm. To the right are the time histories measured by the probes with the number-2 turboprop engine shut down and with the propeller feathered. For the latter case, at a forward aircraft speed of 130 knots, the propeller does not rotate. As is evidenced by the traces with the engine operating, there is a pronounced disturbance caused by the passage of the propeller blades. The magnitude of the sensor response decreases with distance away from the propeller tip, but is clearly seen by sensor B, which is located at the centerline of the JT15D-1 engine. In contrast, the hot-film time histories with the engine shut down show no periodic disturbance, but rather a low-level, random atmospheric turbulence as expected. Because of the existence of a significant periodic propeller-wake-related distortion across the proposed inlet plane, the OV-1B Mohawk was operated with the number-2 turboprop engine shut down and the propeller feathered during all research flight testing.

Aircraft-Engine Buildup, Instrumentation, and Recording System

After receipt of the modified aircraft, LaRC installed a laser cube on the underside of the aircraft nose cap, installed the modified research engine, installed a signal-conditioning and data-recording system, modified the rudder control lines, and installed an aircraft nose boom and other aircraft-state measurement devices. The resulting research flight vehicle is shown in figure 6 with the number-2 turboprop engine shut down, simulating a research configuration flyover.

The flight experimental engine-nacelle assembly is shown schematically in figure 7. This experimental assembly consisted of the JT15D-1 modified engine (see appendix A) with additional instrumentation added, a NASA designed and fabricated bypass exhaust nozzle with acoustic treatment, and a NASA designed and fabricated research flight inlet. To insure data compatibility, identically modified JT15D-1 engines and inlet hardware designs were used for testing at all three NASA Centers (LaRC, LeRC, and ARC). Since measurement of the forward-radiated inlet noise was the primary concern, means for reducing the aft-radiated, bypass duct noise were employed at all three Centers. However, test fixtures and schedule constraints forced some differences in the hardware used by each Center. Each different acoustic treatment configuration for exhaust noise is addressed in the subsequent sections of this report and each of the tests is described.

Flight acoustic treatment.- To insure that the far-field inlet noise measurements from the flight test were not contaminated by aft-radiated fan noise, sound-absorbing treatment was placed along the outer wall of the bypass-duct exhaust nozzle. (See fig. 7.) Figure 8(a) is a photograph of the flight bypass exhaust duct with the acoustic treatment installed in the engine, figure 8(b) is a cross-section sketch of the sound-absorbing wall, and figure 8(c) is a measured flight result. The acoustic treatment consisted of nine layers of Dupont Kevlar-29 polyamide fiber compressed to a density of approximately 6.2 lb/ft^3 between a perforated aluminum-alloy inner plate (fig. 8(a)) and a solid aluminum-alloy outer plate. The perforated plate had an open area of about 33 percent and, in combination with the solid backing, was designed to attenuate tones at or near the blade-passage frequency (BPF). The Kevlar, a felt-like, bulk-absorbing, synthetic fiber, was installed for broadband noise attenuation.

Flight tests were conducted both with and without the acoustic treatment. Noise reduction was achieved for all angles aft of 80° from the engine front centerline axis. A spectral comparison for a radiation angle of 110° is shown in figure 8(c). The acoustic treatment produced a 10-dB noise reduction at the BPF tone. In addition, a broadband noise reduction of about 5-dB was achieved over most of the frequency range. Higher frequency tones, far from the design point, were relatively unaffected.

Test-engine inlet.- One of the basic criteria to insure successful data comparison required a commonality of hardware. Because it was indicated in reference 5 that the inlet duct contour may have considerable effect on the directivity of forward-radiated fan noise, it was decided that the same inlet lip and internal contour lines would be used for each of the static, wind-tunnel, and flight tests. To accomplish this, a research inlet was designed by LeRC which would perform as well for the static tests as it would for cruise conditions in the flight tests.

The inlet contour chosen was based on the results of work that had been done for the Quiet Clean Short-Haul Experimental Engine (QCSEE) high Mach number inlets at LeRC. As shown in figure 7, the inlet has essentially the same internal contours as the production Cessna Citation inlet from the throat (19.900-in-diameter cylindrical section) back to the fan case. From the throat forward to the inlet highlight, the internal lip is a 2 to 1 ellipse with a 1.46 contraction ratio. Using the highlight of the production Cessna inlet lip (station number 20.500) as $x = 0$, the contour of the internal lip from the point where it joins the Cessna inlet ($x = 1.05$; station 21.55) to the lip highlight ($x = -3.09$; station 17.411) is written as

$$\left(\frac{x - 1.05}{4.14}\right)^2 + \left(\frac{y - 12.02}{2.07}\right)^2 = 1$$

or

$$y = 12.02 - 2.07\left[1 - \left(\frac{x - 1.05}{4.14}\right)^2\right]^{1/2}$$

for $-3.09 \leqslant x \leqslant 1.05$. From the inlet highlight outward, the lip is a 2 to 1 ellipse with the curvature at the highlight matched and the tangency point the same as on the Cessna nacelle. The contour of the external lip from the lip highlight ($x = -3.09$) to the point where the tangent of the curve becomes horizontal ($x = 24.5$) is written as

$$\left(\frac{2.45 - x}{27.59}\right)^{3.36} + \left(\frac{y - 12.02}{4.12}\right)^2 = 1$$

or

$$y = 12.02 + 4.12\left[1 - \left(\frac{24.5 - x}{27.59}\right)^{3.36}\right]^{1/2}$$

for $-3.09 \leqslant x \leqslant 24.5$. The inlet design performance was checked with existing computer programs at LeRC. Two analytical computer programs were used. One considered the compressible potential flow, and the other considered the boundary layer. The following operating conditions were considered: total engine-air weight flows of 49 and 75 lb/sec for a forward speed of 100 knots, and for a static condition (2 to 3 knots). The weight flow of 49 lb/sec was chosen in order to obtain a fan-rotor rpm where the rotor-alone sound field is cut off. The weight flow of 75 lb/sec is the maximum engine airflow. The results of these analyses showed that the designed inlet was capable of unseparated flow statically and was capable of satisfactory flight performance.

Inlet and engine instrumentation.- Figure 9 is a drawing of the flight research inlet. It shows the locations of 3 Kulite pressure transducers and 32 static-pressure ports which were used to study the noise in the inlet and the aerodynamic performance of the inlet, respectively. The three Kulite transducers were placed at locations upstream of the fan to determine if an acoustic tone was present for different test-engine rpm's. The placement of the static ports was chosen to measure the behavior of the flow in the inlet lip region, including the inlet stagnation point, and the pressure profiles along an axial line on the inner wall of the inlet. The eight circumferential static ports at nacelle station 30.000 provided data to calculate the total mass flow through the engine. Appendix B gives the basis for the derivation of formulas to calculate the engine performance. Appendix C shows the actual output of the digital recording system and shows how these static-port measurements were used to calculate engine and aircraft performance.

In the section entitled "Flight Results and Comparisons," data are presented to show comparisons of static, wind-tunnel, and flight inlet inflow behavior with the static-pressure measurements in the inlet.

In addition to the engine transducers installed during the modification of the test engine (see appendix A), NASA added the aforementioned 3 inlet Kulite transducers, 64 pressure transducers, over 20 engine-bypass-duct temperature transducers, and a JT15D-1 fuel-flow transducer. Additional aircraft instrumentation measured angles of attack and sideslip, total and static pressure (all from the nose boom), and the rpm's of shaft components of all three engines. Numerous other transducers measured parameters for monitoring aircraft and test-engine operation.

Data recording system.- The data recording system employed a combination of analog and digital data-acquisition techniques. Table 2 is a digest of the instrumentation-system characteristics. Figure 10 is a block diagram of the system. Details of the instrumentation system and its operation aboard the aircraft are contained in reference 18.

Figures 11 and 12 identify the location of the most important components of the system and serve to demonstrate its complexity. The control of the system required a full-time instrumentation operator aboard the aircraft. His job was to coordinate the trimming of the JT15D-1 engine speed, to keep a real-time log, to initiate the operation of the telemetry and data recording systems, to deenergize the systems at the appropriate time, and to coordinate all these activities with the pilot, who maintained the flight parameters constant during the aircraft flyover of the microphone array.

WIND-TUNNEL TEST DESCRIPTION

Tests with the modified JT15D-1 engine were performed jointly by LaRC and ARC personnel at the Ames 40- by 80-Foot Wind Tunnel and the Ames Outdoor Static Test Stand. The purposes of the tests were to collect data to affirm that JT15D-1 fan noise can be simulated in a tunnel, to qualify wind-tunnel limitations to guide more accurate static testing of engines, to demonstrate the existence of a clean inflow for the OV-1B/JT15D-1 flight configuration with forward velocity (i.e., effect of OV-1B wing on inlet inflow), and to investigate angle-of-attack effects upon source and far-field noise measurements. Figure 13 is a photograph of the JT15D-1 engine mounted in the wind tunnel. Reference 19 contains the details and results from these tests.

The LaRC flight JT15D-1 engine was used for these tests. The LeRC fan rotor and telemetry nose cone (identical to the LaRC system) were used in the LaRC flight engine. Ames Research Center fabricated the research inlet. The lip and internal contour lines of the inlet were identical to those used at LeRC and LaRC and the external contour line merged smoothly with the wind-tunnel nacelle for the JT15D-1 engine. (See fig. 14.) The test runs performed at the Ames Outdoor Static Test Stand utilized the same engine-nacelle-pylon hardware as was used in the tunnel.

Also shown in figure 14 is the acoustic treatment that was added to reduce the aft-radiated bypass-duct exhaust noise. The acoustic treatment around the core nozzle was contained within a perforated outer aluminum wall. As the original engine exhaust system was fabricated and used for the hybrid-inlet research performed in reference 20, a new cone-shaped outer wall was designed to provide a thick lip ($\approx$1 in.) at the core nozzle exit. This lip acted as a tab for the bypass-duct exhaust to adjust its annular open area close to that of a production JT15D-1 engine.

STATIC-TEST DESCRIPTION

The LeRC conducted static fan tests at their Vertical Lift Fan Facility. The emphasis in the Lewis tests was the development of a passive inlet inflow control device (ICD) to simulate flight noise source behavior in a ground static-test facility. References 21 and 22 contain details of the LeRC program and the outdoor static test facility.

The outdoor test facility at LeRC is shown in figure 15. The JT15D-1 test engine is suspended from a thrust-measuring system on a cantilevered vertical pylon support arm. The engine centerline is 9.5 ft above the ground and 3.4 fan diameters from the nearest test support structure. The photograph shows the JT15D-1 engine configured for baseline acoustic tests using a bellmouth inlet and connected to the exhaust muffler. Both the bypass exhaust gas and core exhaust gas are exhausted into the muffler, which effectively eliminated all aft-radiated noise.

The results have culminated in the successful development of small, simple, and inexpensive ICD design. (See refs. 22 and 23.) Figure 16 is a photograph of the ICD, and figure 17 contains some construction and mounting details. This compact ICD is only two fan diameters across, and, as demonstrated in reference 23, the radiated-noise field is not significantly altered by its presence. Furthermore, it was shown that this new ICD generates no important new noise sources.

FLIGHT RESULTS AND COMPARISONS

This section contains descriptions of some analytical flow-field calculations for the JT15D-1 nacelle inlet and comparisons of the calculated results with measured flight values. Data are presented in terms of static-pressure distributions and various performance parameters (either measured directly or calculated from the measured values) as a function of fan speed. Explicit analytical expressions for several of the parameters are presented in appendix B. Table C1 is a list of symbols to aid in reading a PCM (pulse-code modulated) printout. A typical listing of PCM data is presented in table C2. Finally, a composite fan operating line is shown which compares static, wind-tunnel, and flight results.

Inlet Flow-Field Comparisons

The inlet of the JT15D-1, described in the section entitled "Test-Engine Inlet," was designed to operate over the entire range of test environments: static, wind-tunnel, and flight. To evaluate the aerodynamic design, various inlet flow conditions were exercised using an inviscid, compressible, potential-flow computer program. The program is an advanced version of the procedure described in reference 24, and it generates three-dimensional flow fields about axisymmetric bodies. Input quantities include inlet geometry, weight flow, forward velocity, and angle of attack. Output quantities include the three components of velocity, Mach number, and pressure ratio along the wall.

Figure 18 presents calculated results from the program which display the vector flow fields in the inlet. The calculations were performed for a total engine weight flow of 47.5 lb/sec, which is typical for a landing-approach engine setting and for forward speeds representative of static (<3 ft/sec), wind-tunnel (100 ft/sec), and flight (220 ft/sec) test conditions. For these vector plots, the length of the vector indicates speed scaled to the length of a grid which corresponds to 1000 ft/sec. In figure 18(a), which is for the static-test case, it is seen that airflow is drawn into the inlet from all directions in an environment initially at rest. The flow field reveals a rapid acceleration around the inlet lip and a quick adjustment to near-uniform flow not far into the inlet. The wind-tunnel flow field of figure 18(b) indicates that the inlet flow is drawn in from the forward direction but with less acceleration than for the static case in the region of the highlight. The flight-test environment of figure 18(c) shows a near-uniform flow field, little accelerated flow, and the stagnation point occurring near the inlet highlight.

Comparisons of static, wind-tunnel, and flight surface-pressure ratios and Mach number distributions along the inlet wall are presented in figure 19. These data are for the same operating conditions as in the previous figure. The change in stagnation point ($p_s/p_t = 1$) and the different flow gradients in the inlet lip region are evident. However, a quick recovery for all test environments is obtained with the inlet, as evidenced by the close agreement of surface conditions at an internal distance from the highlight of about 5 in. A near matching of conditions is reached about 10 in. aft of the highlight. The fan is located about 30 in. aft of the highlight. Boundary-layer calculations showed that the boundary-layer thickness at the fan varied from 0.39 in. for the flight case to 0.46 in. for the static case.

Inlet Static Pressures

Figure 20 presents surface-pressure-ratio data obtained in flight compared with calculated results. These results are for an axial array of static ports at the bottom of the inlet. The two cases shown correspond to different inlet weight flows. Although the data are not precisely at the same conditions as the calculations, good agreement is obtained for both pressure-ratio magnitude and for the shape of the inlet-wall axial distribution. The region of the inlet just aft of the lip highlight shows the most rapid adjustments. Finally, there is a good match at station 30, where the performance calculations are made.

Calculated circumferential pressure distributions at station 30 for various angles of attack in flight are presented in figure 21. For the axisymmetric inlet used in the analysis, there is a uniform distribution at $\alpha_i = 0°$. As the angle of attack increases, the distortion increases accordingly, as is evidenced by the calculations for $\alpha_i = 6°$ and $\alpha_i = 9°$. Also shown in this figure are the results from a flight test for which the engine total weight flow and aircraft forward velocity are near the values used for the analytical calculations. The flight inlet is axisymmetric with respect to the internal inlet contours, but it is not axisymmetric with respect to the external nacelle contours. The magnitude of the distortion is greater than the predicted magnitude, and there is evidence of a perturbation (148°30') which is not present in the calculated results. Figure 22 shows a series of circumferential pressure distributions from the flight data corresponding to the JT15D-1 fan speeds typically used in the flight test. These distributions indicate that the aforementioned perturbation distortion pattern (148°30') varied with the engine speed, and the greatest deviation was at the lowest engine rpm.

In addition, the analysis showed that at any given angle of attack, the distortion magnitude increased as either aircraft Mach number or weight flow increased. The analysis further showed that the magnitude of the distortion

$$(p_s/p_t)_{max} - (p_s/p_t)_{min}$$

normalized to the inlet Mach number (which is proportional to weight flow) was approximately a linear function of the crossflow component, $M_{ac} \sin \alpha$, in the inlet. This analytical relationship is presented in figure 23, along with flight data over a wide range of weight flow, forward speed, and angle of attack. The flight data do not follow the trends predicted by the analysis. The data indicate a near-constant distortion level that is independent of aircraft speed and inlet angle of attack. This result is in agreement with that of reference 25, for which the inlet distortion was measured at $\alpha = 0°$ in the wind tunnel. Hence, there appears to be a built-in distortion flow to the JT15D-1 engine which is of sufficient magnitude to mask the smaller distortion that is induced by angle of attack. Steady distortions in an inlet, of course, can represent a noise source.

Variations of Operating Parameters With Fan Speed

Flow incidence angle of the fan relative to the tangent angle at the blade-tip leading edge (72°) was calculated from the vector sum of the mean flow in the inlet at the fan face M_f and the rotor-tip Mach number M_t; that is,

$$\alpha_{t,rel} = 72° - \arctan(M_t/M_f)$$

where $M_t = \pi d_f N_1/60c$, d_f is the duct diameter at the fan face, and c is the speed of sound. Calculated results comparing static and flight data over a range of fan speeds are presented in figure 24. Both sets of data show increasing incidence angle with fan speed. Static data show larger angles at all speeds. The difference is due primarily to stagnation-pressure differences (required to calculate M_f) that arise between tests conducted statically and during flight. A major contributor to the broadband noise spectrum may be the interaction between the rotor and the inlet boundary-layer turbulence (ref. 26). This mechanism is a direct function of rotor leading-edge loading, which is a function of incidence angle. It is shown in reference 26 that blade-tip relative Mach number and incidence angle are the dominant parameters for predicting broadband noise levels for fans designed to operate in the transonic flow region. For a given engine (e.g., JT15D-1), this implies that broadband noise differences between static and flight tests at the same fan speed (or more precisely the same tip relative Mach number) should be a function of incidence angle alone.

Figures 25 to 30 are data plots of performance parameters from the PCM data of appendix C. The performance data are plotted against the JT15D-1 fan speed N_1. This fan speed is, of course, fundamental in the determination of which tones (blade-passage frequencies) are generated.

Fan Operating Lines

Figure 31 shows a plot of the fan pressure ratio versus corrected total weight flow through the engine which is commonly referred to as the fan operating line. For valid noise comparison it was important to insure that the engine repeated its performance curve during each set of flight tests. Two sets of data from flight tests on 2 different days are shown in figure 31 to demonstrate the excellent repeatability for research operation of the JT15D-1 engine.

Finally, figure 32 is a comparison of typical fan operating curves taken from each of the static, wind-tunnel, and flight tests. The overall comparison between the static and flight-test operating curves is very good. Because the time schedule dictated the use of existing bypass and core exhaust hardware, the wind-tunnel operating curve deviated at the higher weight flow and fan pressure ratios. However, at the weight flow for the approach power engine settings (45 to 50 lb/sec), the comparison between all three curves is satisfactory.

CONCLUDING REMARKS

The development of a research flight-test vehicle that consists of a modified Pratt & Whitney JT15D-1 turbofan engine and a modified Grumman OV-1B Mohawk aircraft is presented in this paper. The static, wind-tunnel, and flight-test hardware and environments are described. It is shown that care was taken to use identical inlet hardware during research testing to assure that valid comparisons could be made between the three data bases.

Comparisons of the flight data with the analytical calculations have demonstrated satisfactory performance of the flight inlet. Repeatability of the fan operating curves for the JT15D-1 test engine during flight was shown to be very good.

The static and flight operating curves are in good agreement over the entire fan operating range. Comparisons of these curves with the wind-tunnel operating curve show good agreement in the range for an approach power setting; that is, at about 10 500 rpm, the wind-tunnel curve is only slightly lower. However, the discrepancies between the operating lines are due primarily to exhaust-system differences, rather than to any engine-inlet differences.

Langley Research Center
National Aeronautics and Space Administration
Hampton, VA 23665
January 27, 1984

TABLE 1.- GENERAL INFORMATION ABOUT OV-1B MOHAWK AIRCRAFT

Wing span, ft	48
Overall length, ft	41
Tail height, in.	152
Aspect ratio	6.11
Fuel capacity, lb (internal)	1930
Power plants (2)	Lycoming T53-L-7
Take-off power, ESHP each	1150
Weight:	
Structure (wing, tail, body, landing gear, nacelles), lb	4425
Propulsion group, lb	2415
Electronics group (including autopilot), lb	1697
Passive defense (armor, flak curtains, bullet-resistant glass), lb	239
Fixed equipment (flight controls, instruments, hydraulics, electrical, furnishings, air conditioning, photographic with V/H scanner, auxiliary gear), lb	2291
Total empty weight, lb	11 067
Crew (2), lb	400
Usable fuel (297 gal), lb	1930
Photographic equipment (camera and accessories), lb	95
Oxygen installation, lb	51
Observer's pack, lb	25
Miscellaneous useful load, lb	181
Total useful load	2682
Take-off gross weight, lb	13 749
Performance:	
Maximum speed at maximum power, knots	259
Maximum speed at 5000 ft, MRP, level flight, 60 percent fuel, knots	250
Stall speed at sea level, landing configuration, 10 percent NPR, knots	70
Take-off distance over 50-ft obstacle, ft	975
Landing distance over 50-ft obstacle with 60 percent fuel, ft	925
Service ceiling at take-off gross weight less 20 percent fuel, ft	25 000
Rate of climb, 2 engines, MRP at sea level and take-off weight, ft/min	2775
Endurance at 200 knots and 5000 ft, hours	1.80
Maximum endurance (two 150-gal external tanks) at 20 000 ft, hours	6.11
Range (two 150-gal external tanks), n.mi.	1094
Time, hours	5.49
Average speed, knots	203
Cruise altitude, ft	20 000

TABLE 2.- JT15D-1/OV-1B INSTRUMENTATION-SYSTEM CHARACTERISTICS

Telemetry:	
Number of pressure channels	8
Frequency response, kHz	0.02 to 20
Signal-to-noise ratio, dB	50
Dynamic range, dB SPL	120 to 170
Frequency range, MHz	60 to 108
Power	Battery/remote controlled
Temperature, °C	-28 to 70
Rotational speed, rpm	16 000
Digital subsystem:	
Number of flight measurements programmed	112
Bits per word	10
Resolution, percent	0.1
Sample rate, sec^{-1}	90
Bit rate, sec^{-1}	100 000
Encoding accuracy, percent full scale	0.4
Wideband FM subsystem:	
Number of channels	21
Center frequency, kHz	104
Deviation, percent	±40
Subsystem accuracy, percent full scale	2
Frequency response, kHz	0.02 to 20
Other subsystems:	
Tape recorders (2), in/sec, direct record	30
Time code, kHz	IRIG-A-10

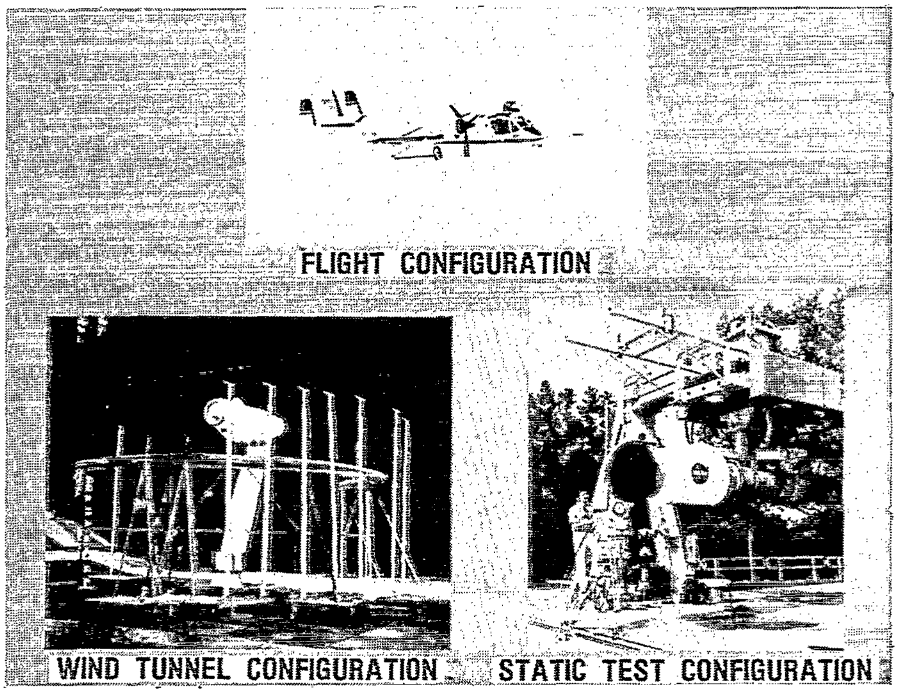

L-83-3467

Figure 1.- Flight effects on fan noise with JT15D-1 test engine.

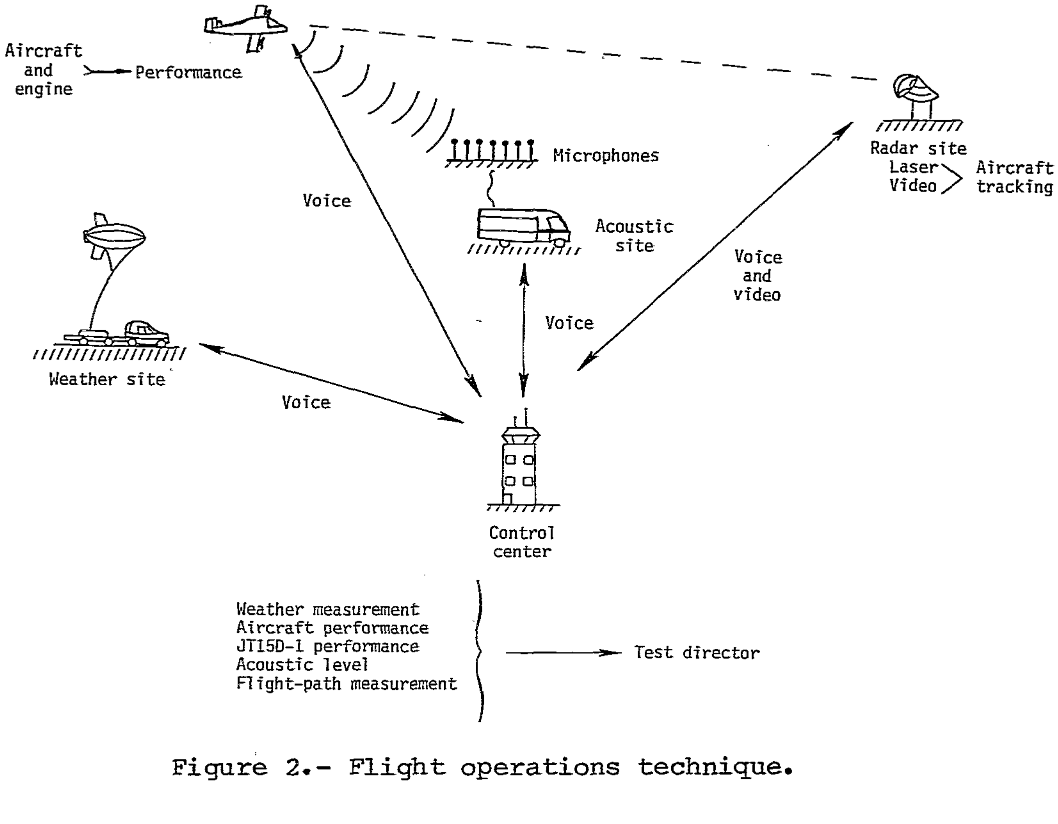

Figure 2.- Flight operations technique.

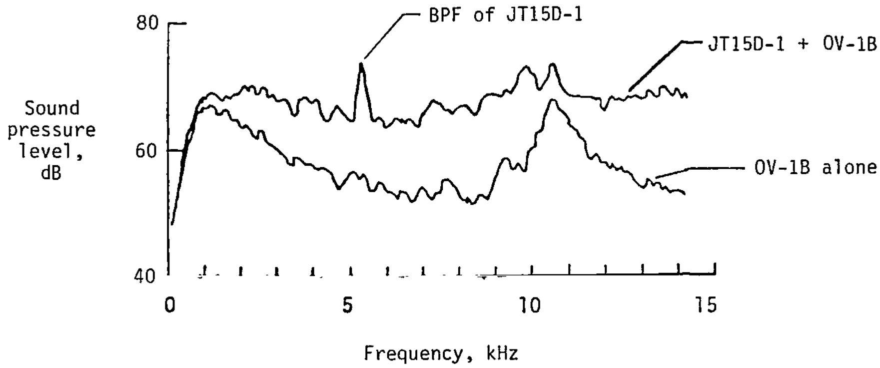

Figure 3.- JT15D-1/OV-1B signal-to-noise ratio. $N_{1,corr} \approx 10\ 800$ rpm; $V_\infty \approx 130$ knots; $\theta_{em} = 60°$; Alt ≈ 300 ft.

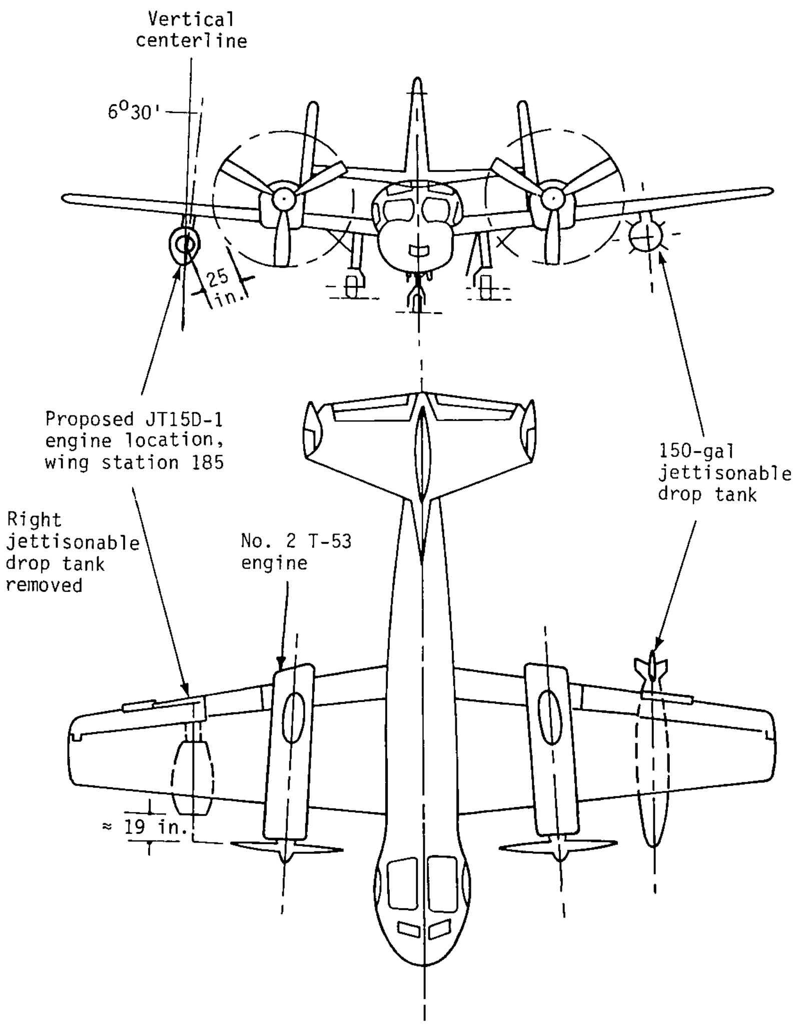

Figure 4.- JT15D-1/OV-1B test aircraft configuration.

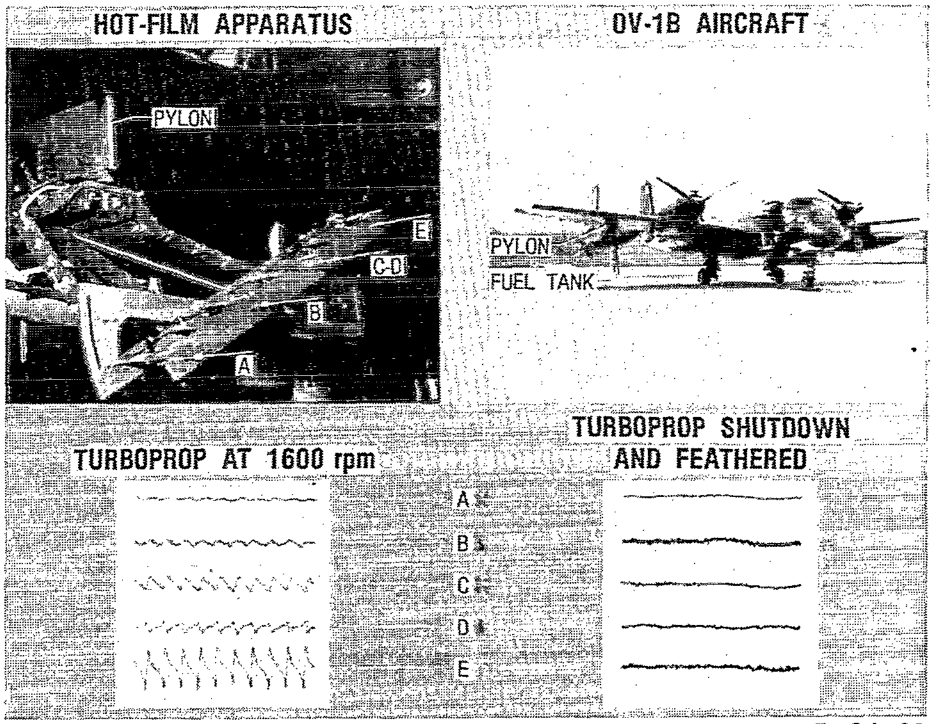

L-84-08

Figure 5.- Hot-film flight test on OV-1B aircraft.

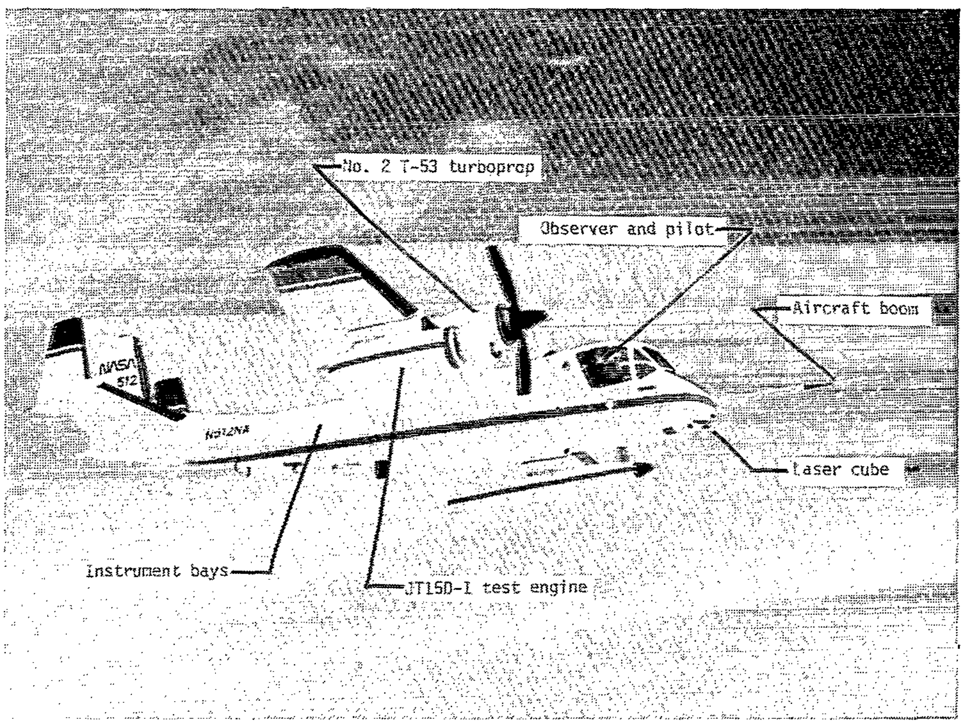

L-81-10,424.1

Figure 6.- Modified OV-1B Mohawk research aircraft in flight.

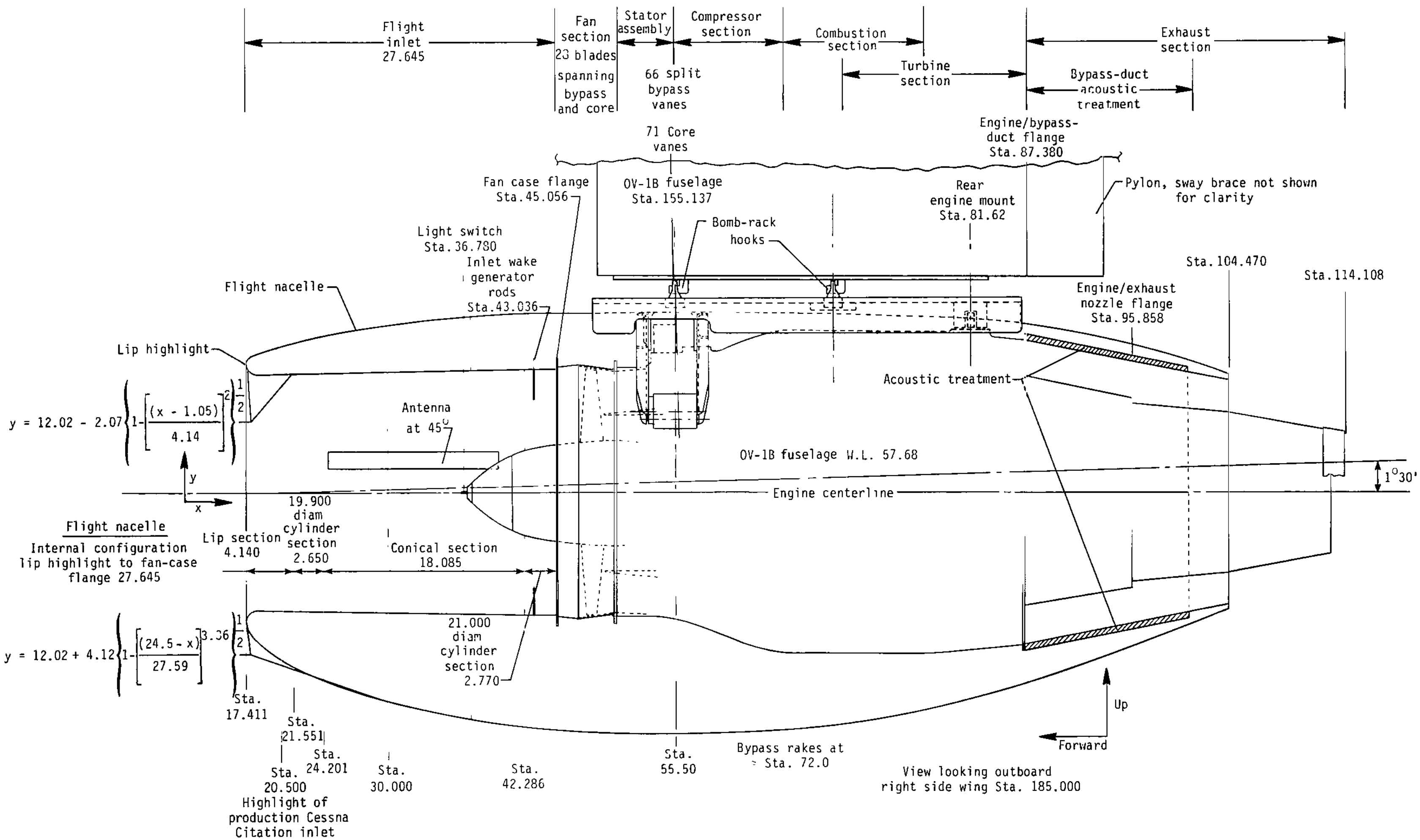

Figure 7.- JT15D-1 engine-nacelle schematic. Linear dimensions are in inches.

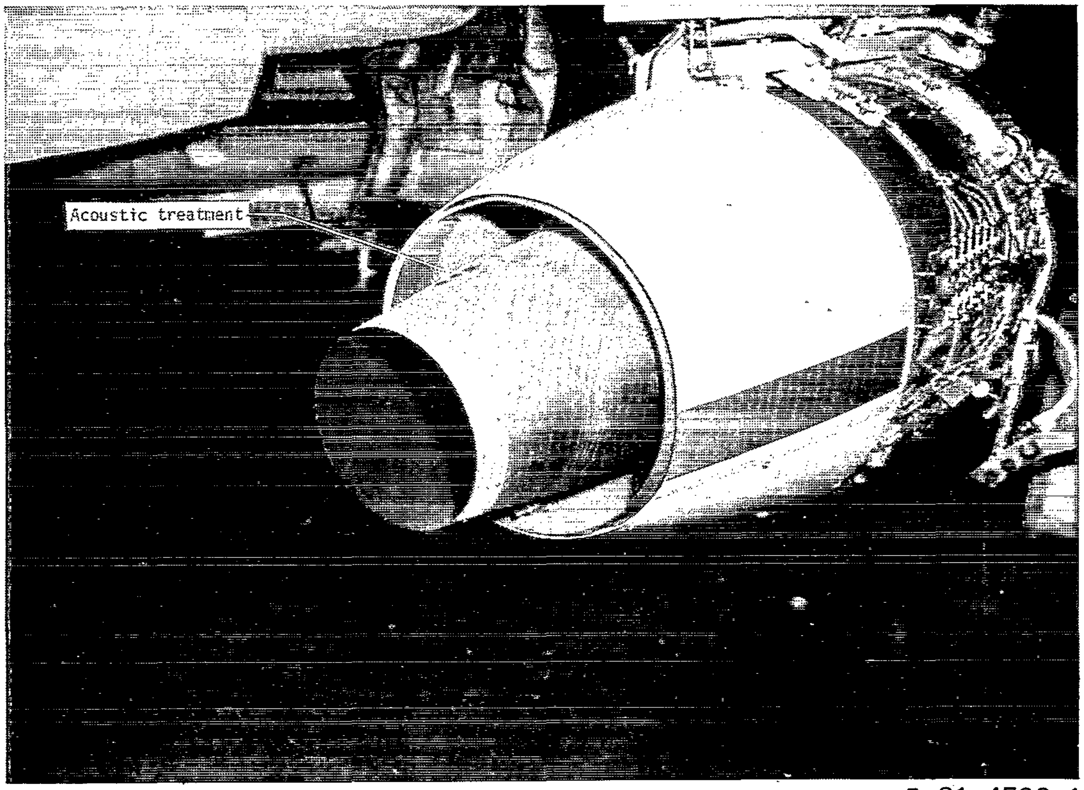

L-81-4703.1

(a) Aft view of JT15D-1.

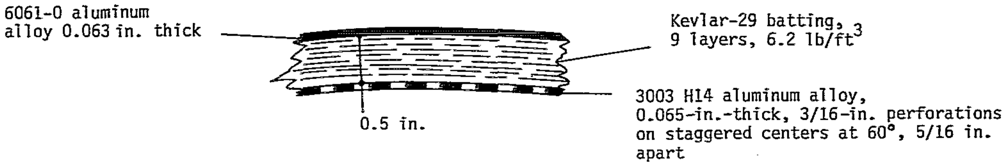

(b) Cross-section diagram of acoustic treatment.

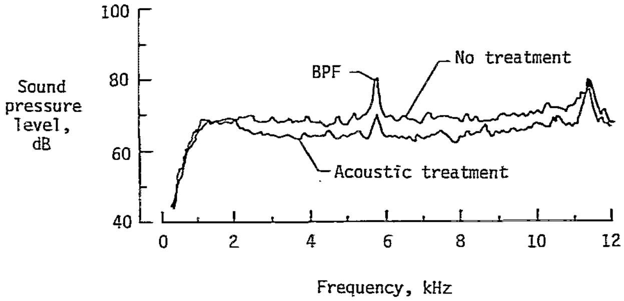

(c) Far-field noise; 110° radiation angle.

Figure 8.- Flight acoustic treatment.

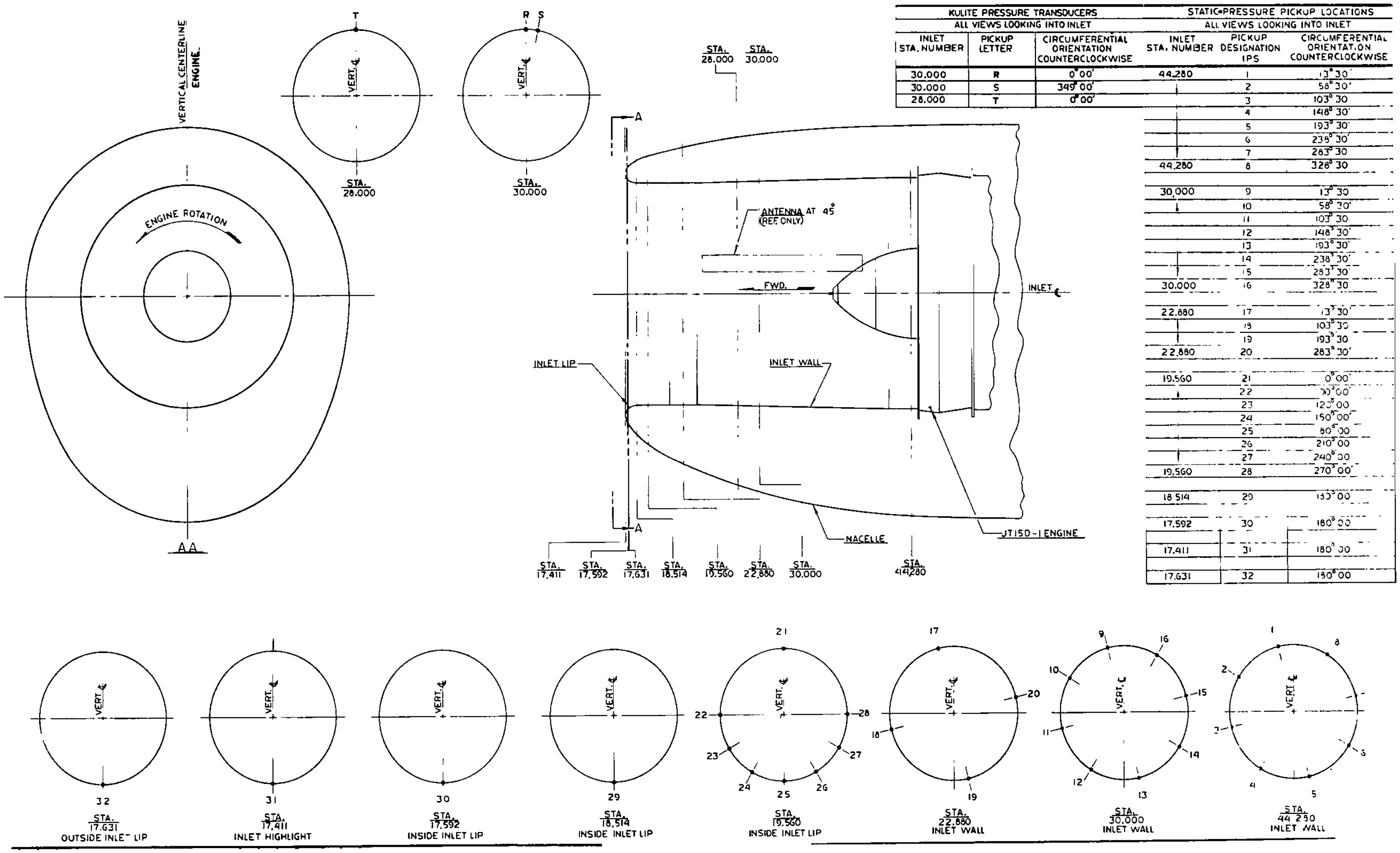

KULITE PRESSURE TRANSDUCERS		
ALL VIEWS LOOKING INTO INLET		
INLET STA. NUMBER	PICKUP LETTER	CIRCUMFERENTIAL ORIENTATION COUNTERCLOCKWISE
30.000	R	0° 00'
30.000	S	349° 00'
28.000	T	0° 00'

STATIC-PRESSURE PICKUP LOCATIONS		
ALL VIEWS LOOKING INTO INLET		
INLET STA. NUMBER	PICKUP DESIGNATION IPS	CIRCUMFERENTIAL ORIENTATION COUNTERCLOCKWISE
44.280	1	13° 30'
	2	58° 30'
	3	103° 30
	4	148° 30'
	5	193° 30'
	6	238° 30'
	7	283° 30
44.280	8	328° 30
30.000	9	13° 30
	10	58° 30'
	11	103° 30
	12	148° 30'
	13	193° 30'
	14	238° 30'
	15	283° 30'
30.000	16	328° 30
22.880	17	13° 30'
	18	103° 30
	19	193° 30
22.880	20	283° 30'
19.560	21	0° 00'
	22	90° 00'
	23	120° 00
	24	150° 00'
	25	180° 00
	26	210° 00
	27	240° 00
19.560	28	270° 00'
18.514	29	150° 00
17.592	30	180° 00
17.411	31	180° 00
17.631	32	180° 00

Figure 9.- Research inlet static port locations. Linear dimensions are in inches.

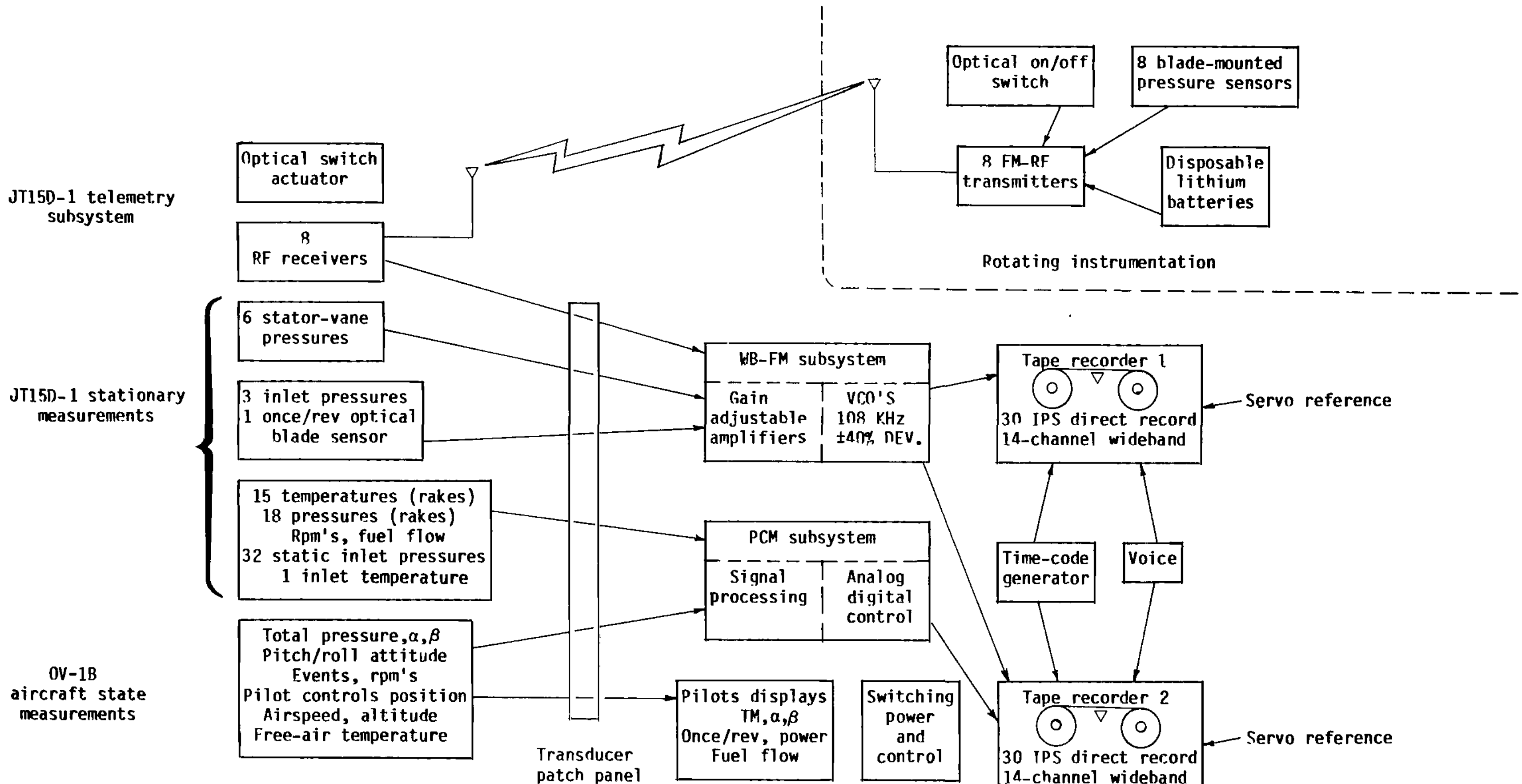

Figure 10.- JT15D-1/OV-1B flight instrumentation.

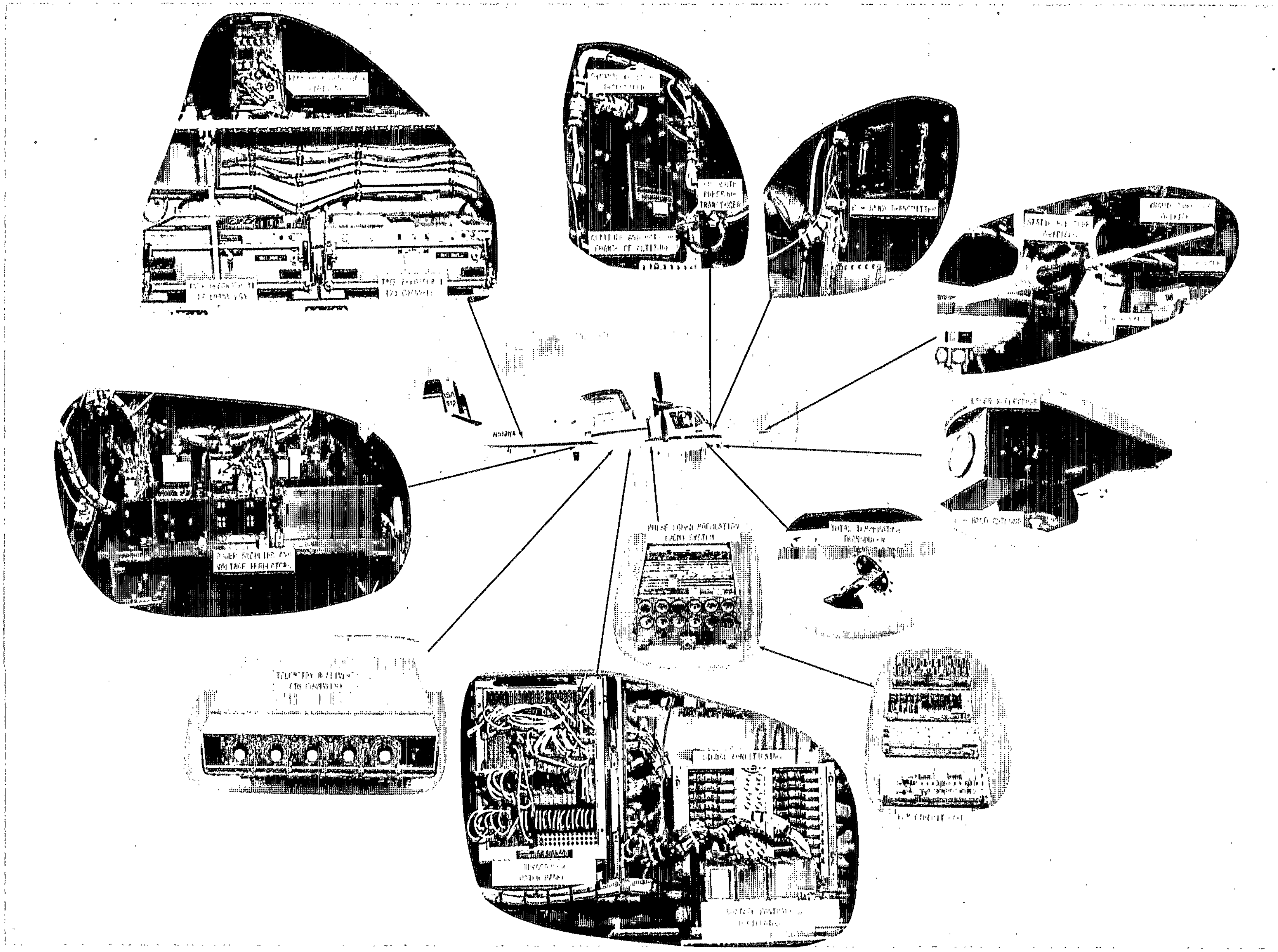

L-83-3641.1

Figure 11.- JT15D-1/OV-1B instrumentation system.

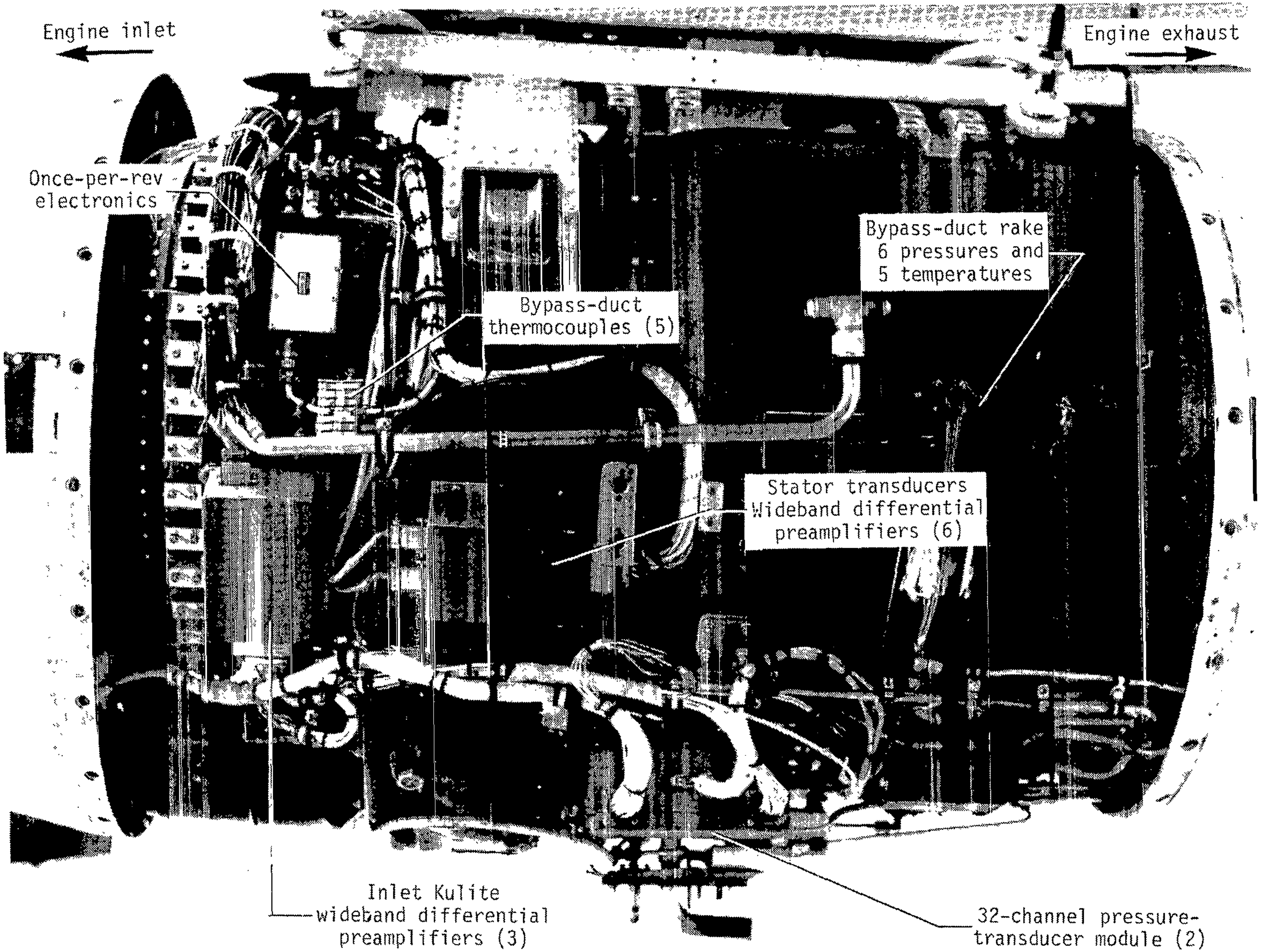

(a) Left side.

Figure 12.- JT15D-1 engine research instrumentation.

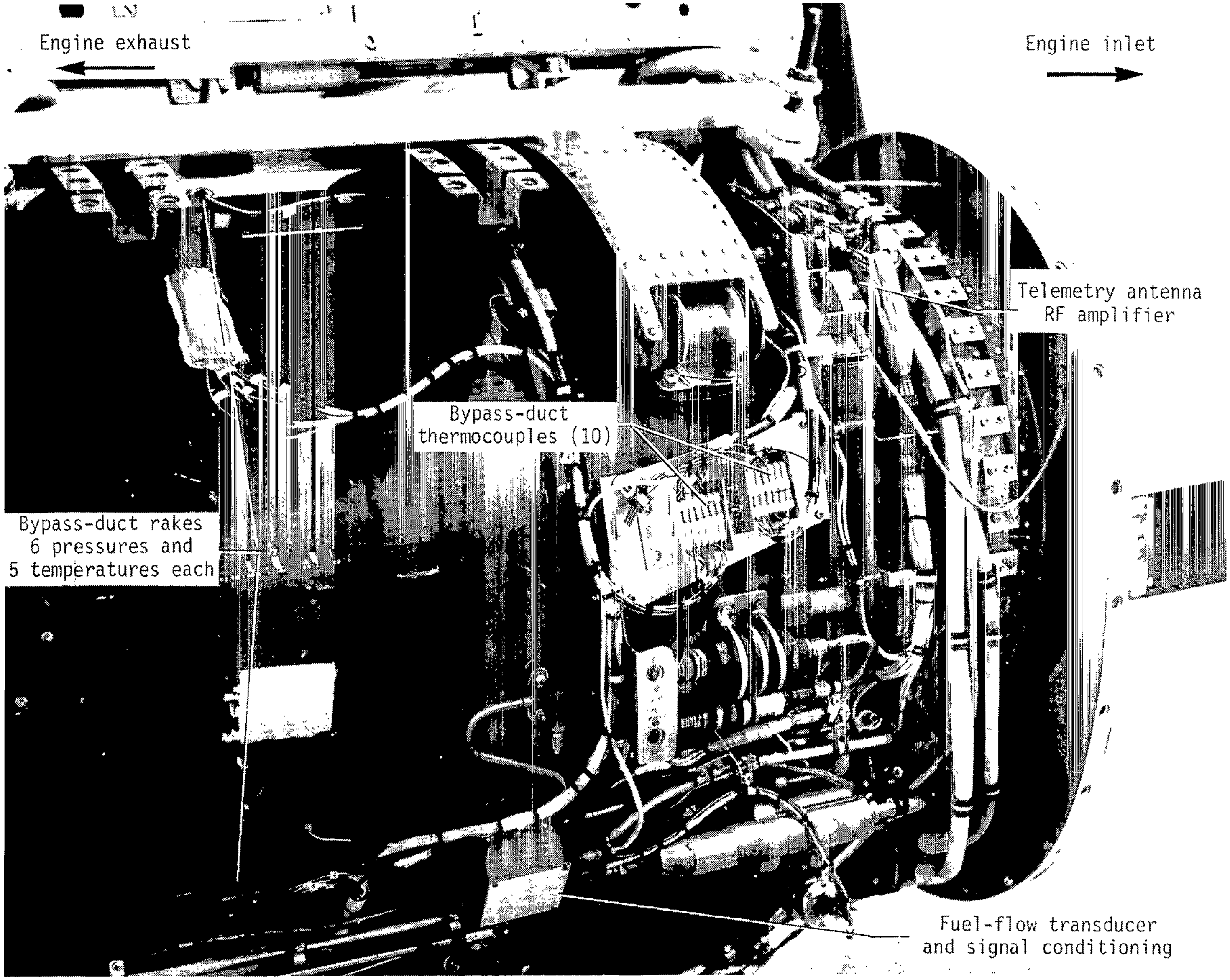

L-82-9241.1

(b) Right side.

Figure 12.- Concluded.

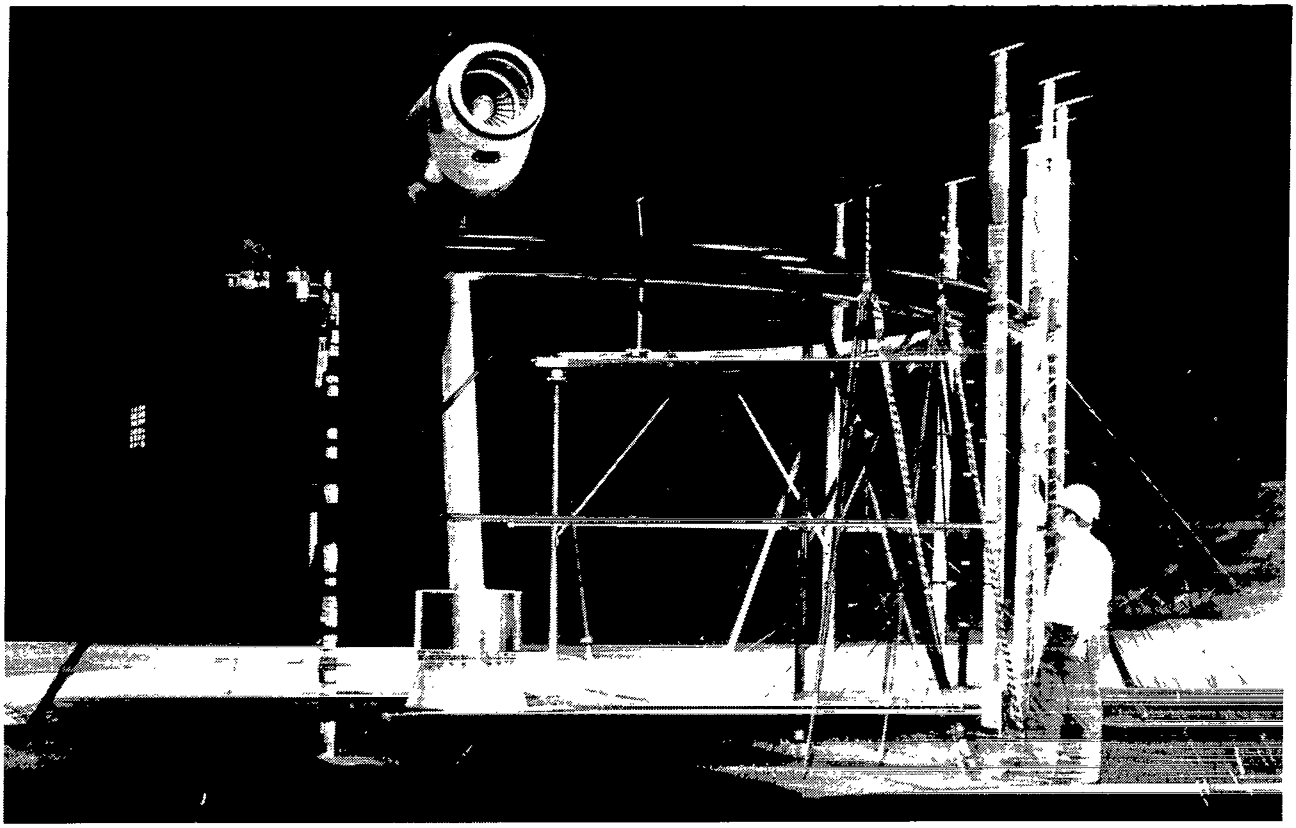

L-84-09

Figure 13.- JT15D-1 noise test in Ames 40- by 80-Foot Wind Tunnel.

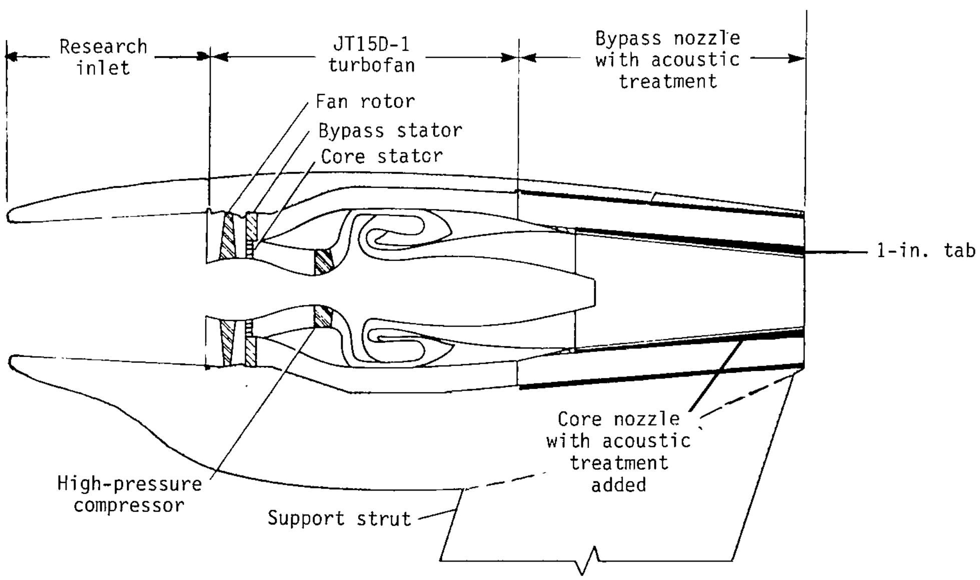

Figure 14.- JT15D-1 engine-nacelle acoustic treatment for test in Ames 40- by 80-Foot Wind Tunnel.

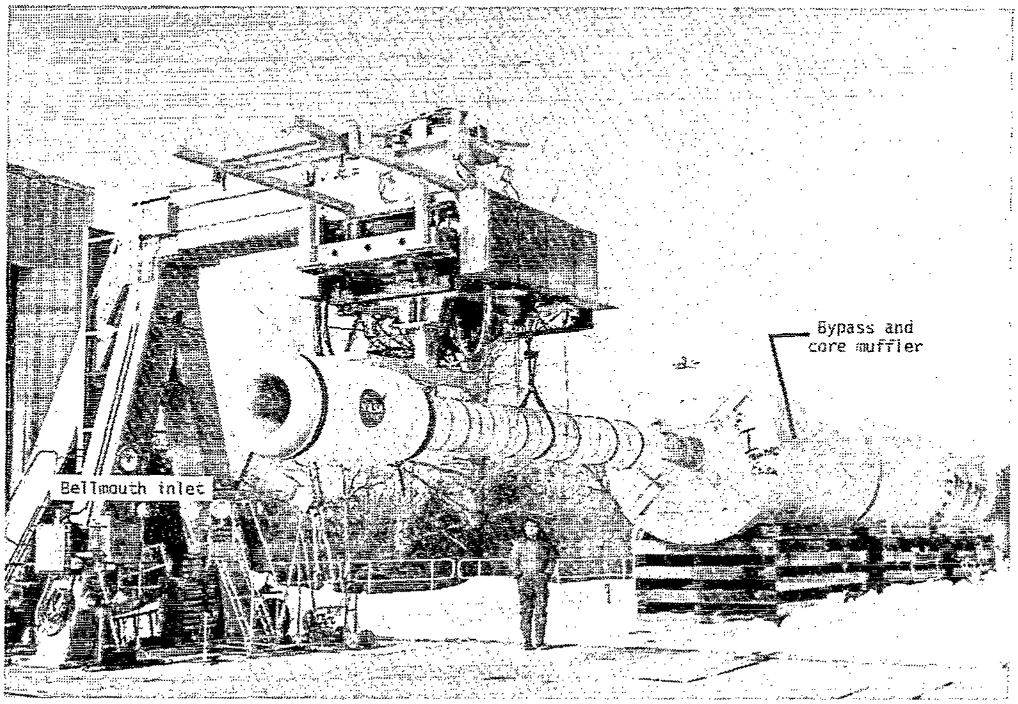

C-78-739

Figure 15.- JT15D-1 engine at Lewis Vertical Lift Fan Facility configured for baseline acoustic tests.

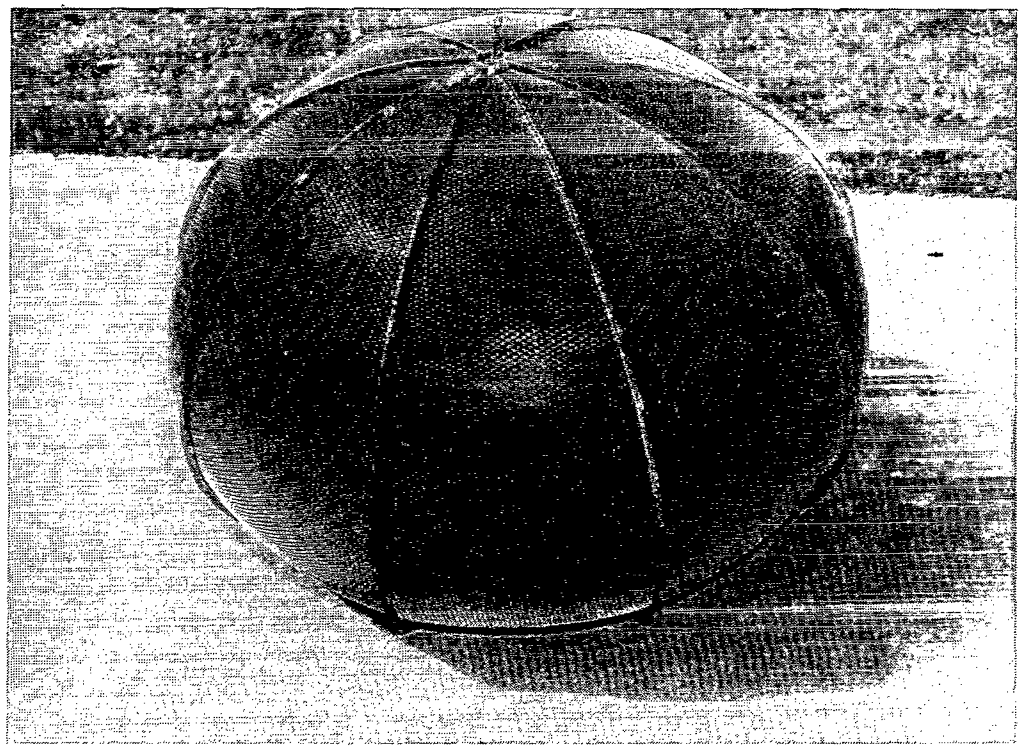

C-81-3429

Figure 16.- Inlet control device (ICD) number 12.

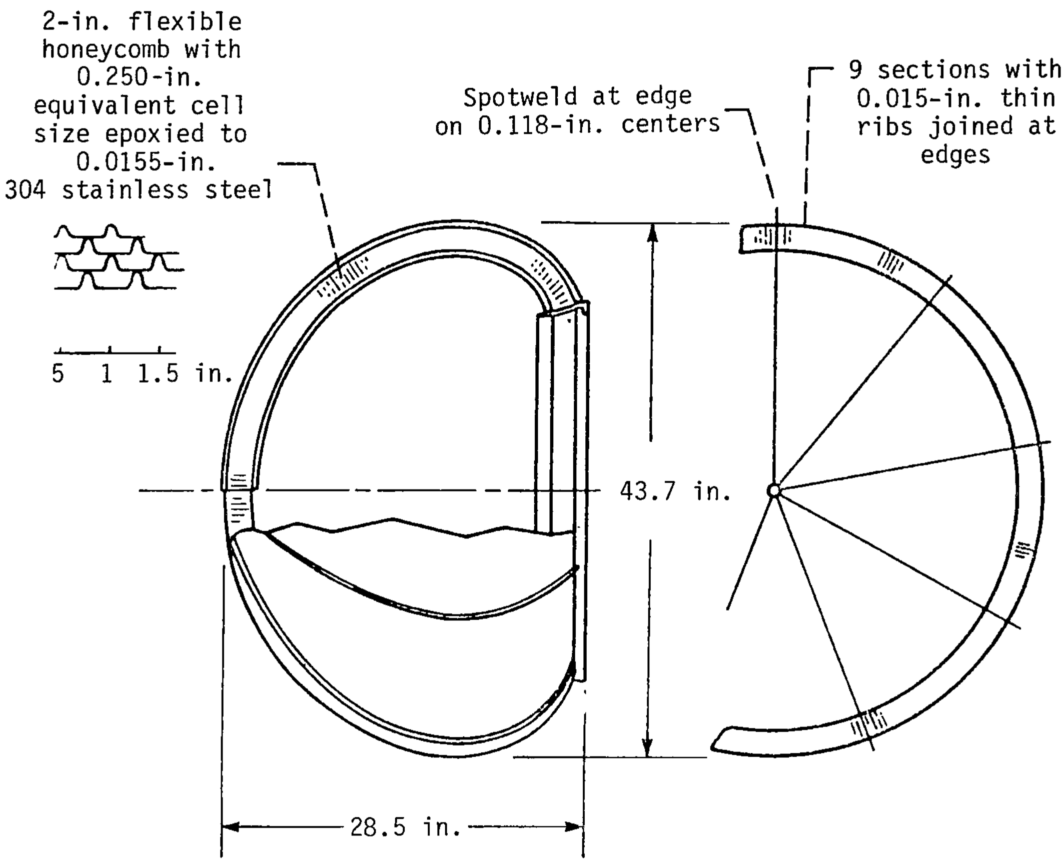

(a) ICD design details (2-fan diam).

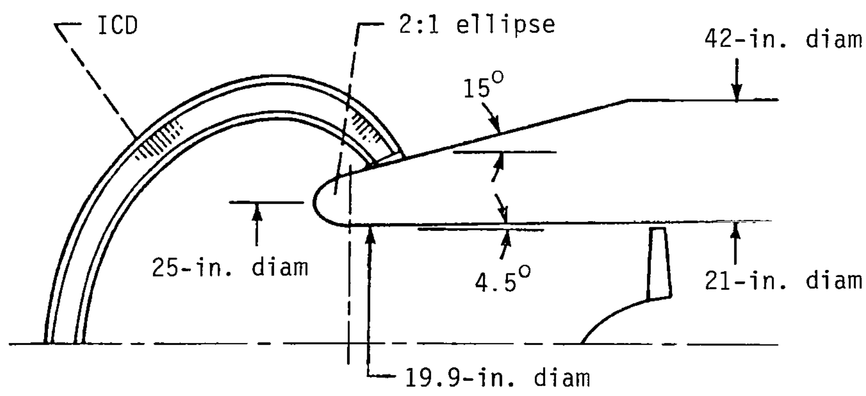

(b) Construction details.

Figure 17.- Construction and mounting details of inlet control device (ICD) number 12.

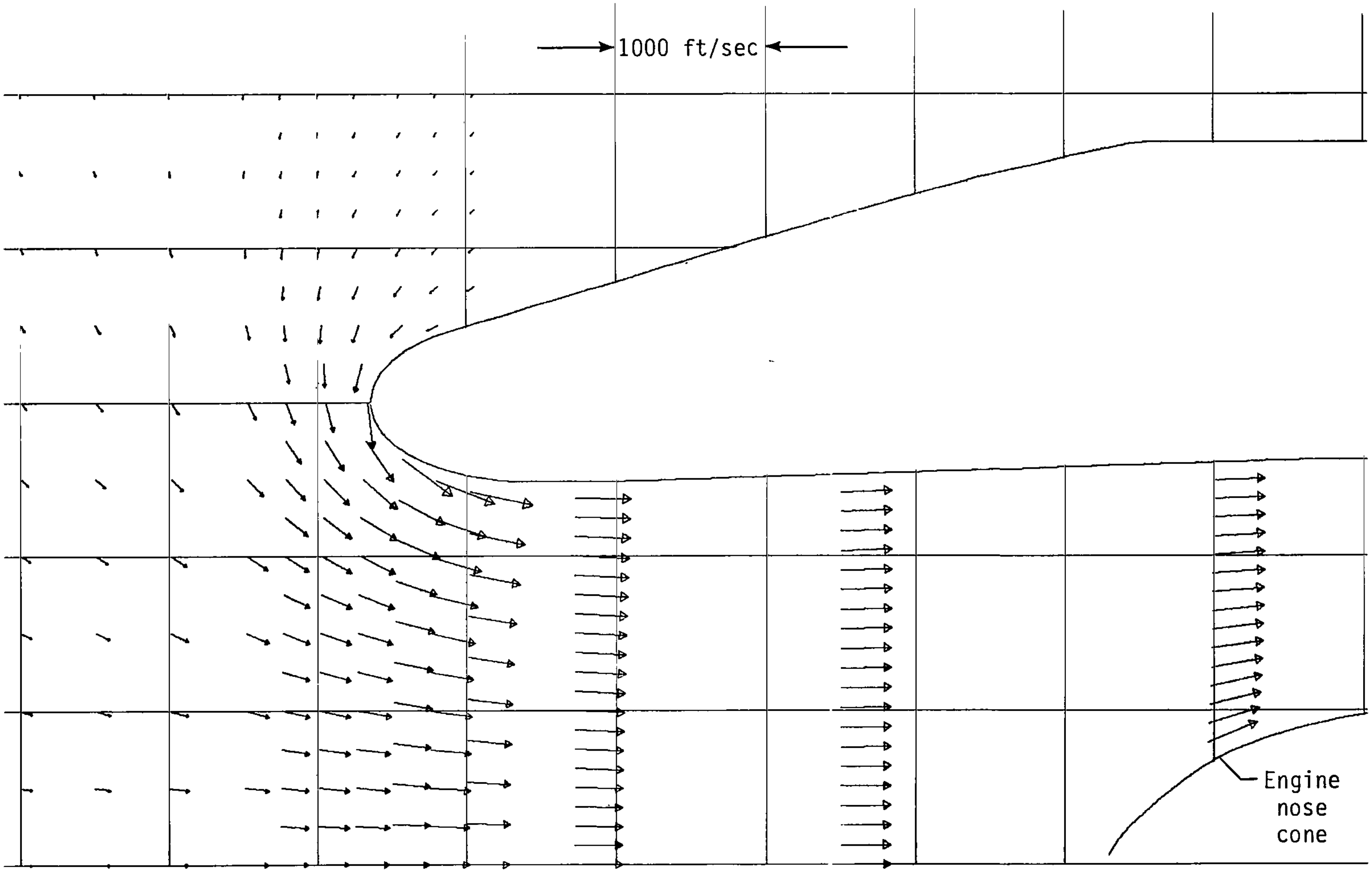

(a) Static conditions.

Figure 18.- Vector flow field for JT15D-1 flight inlet.

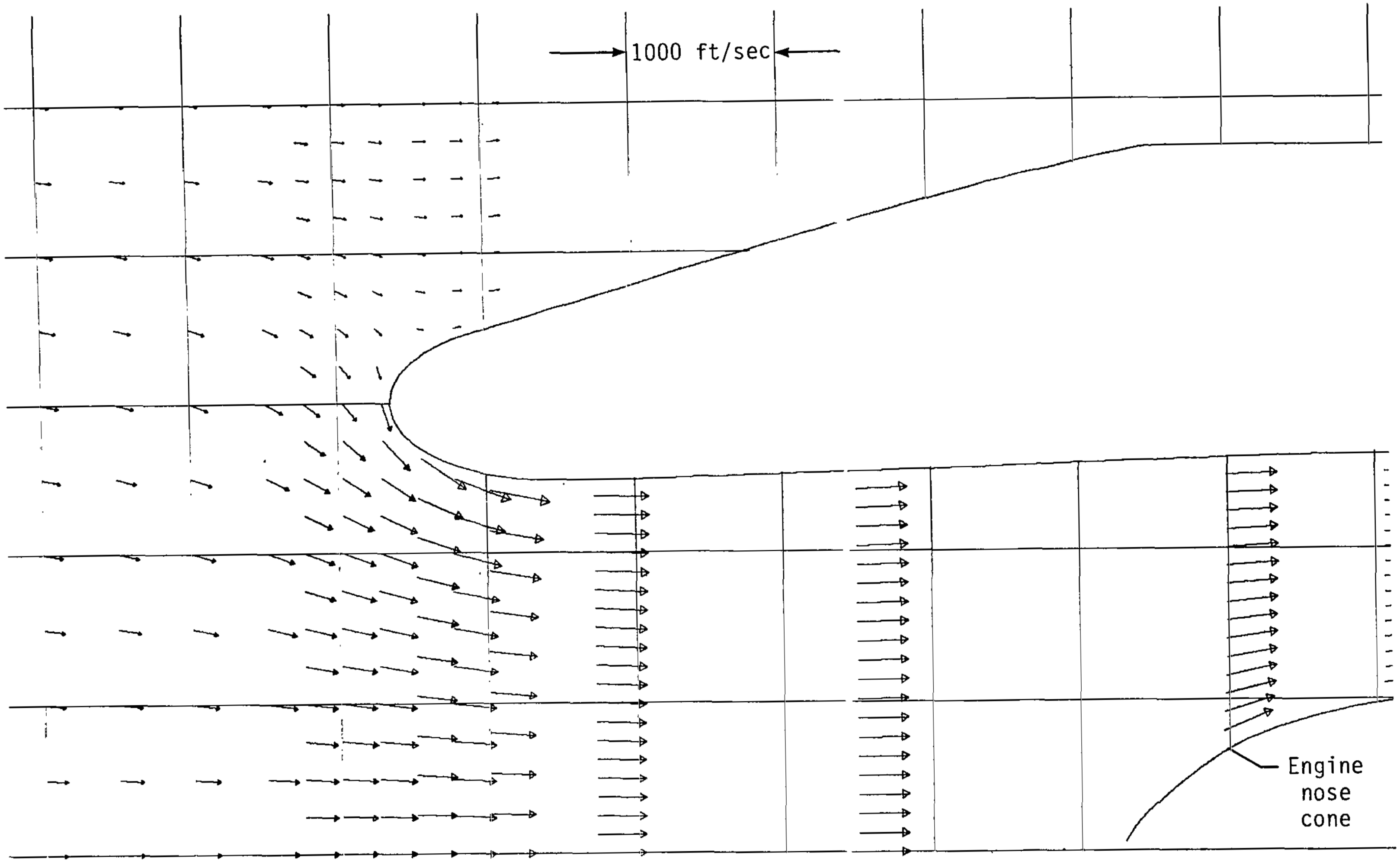

(b) Wind-tunnel conditions.

Figure 18.- Continued.

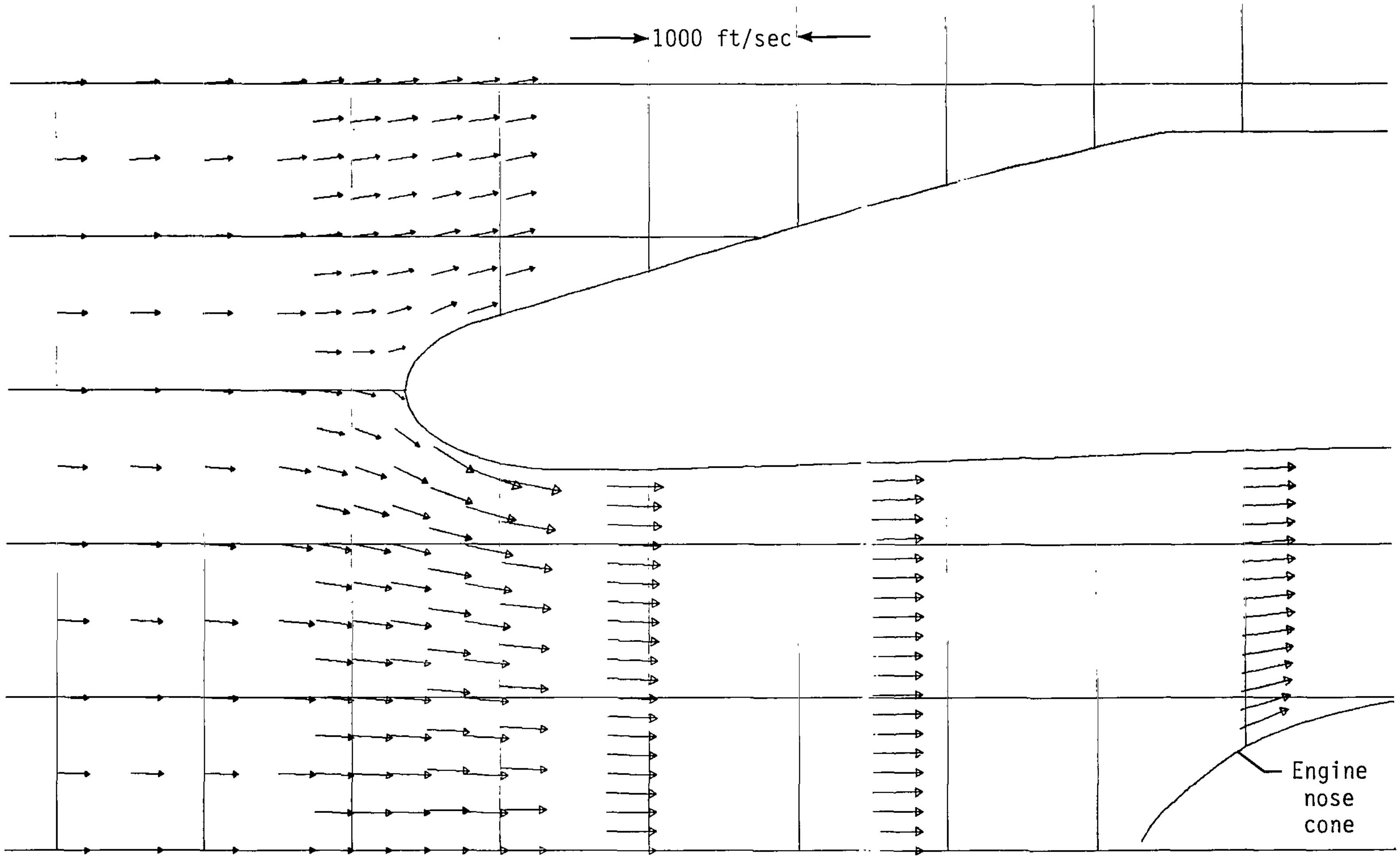

(c) Flight conditions.

Figure 18.- Concluded.

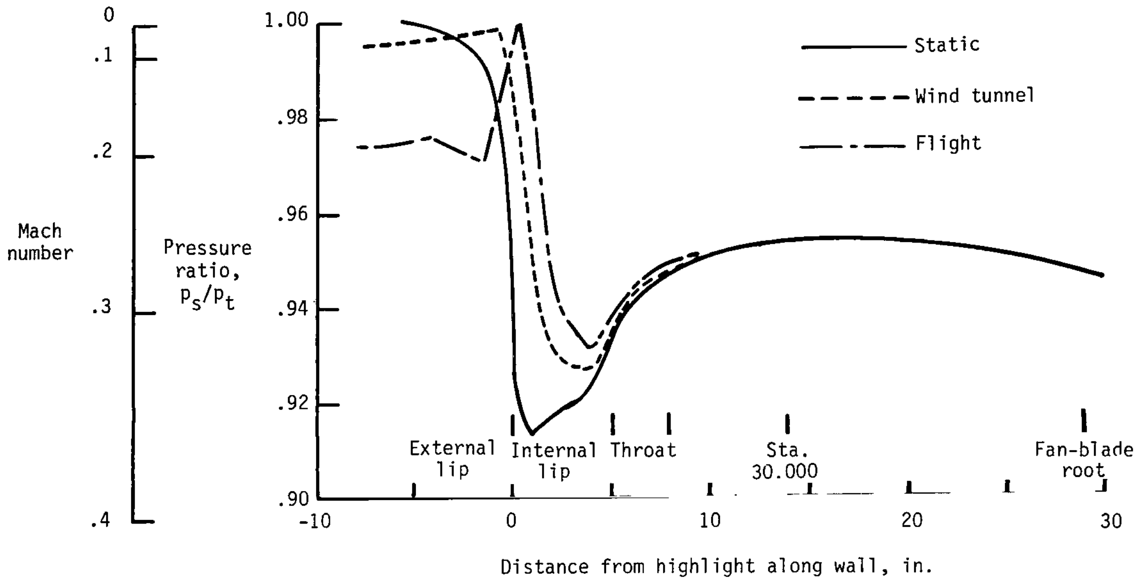

Figure 19.- Comparisons of static, wind-tunnel, and flight pressure and Mach number distributions for $w_{corr} \approx 47.5$ lb/sec.

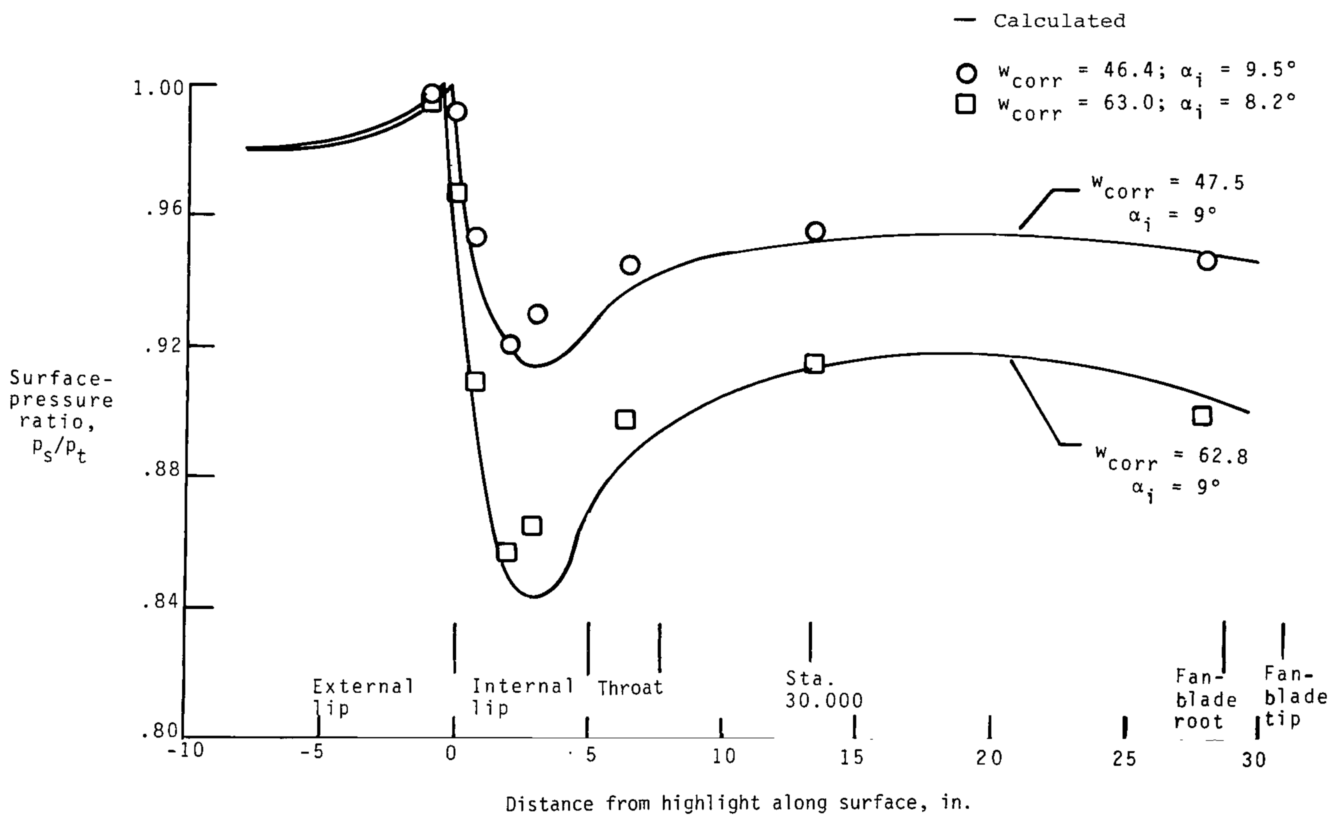

Figure 20.- Comparison of surface-pressure-ratio distributions during flight for different inlet weight flows.

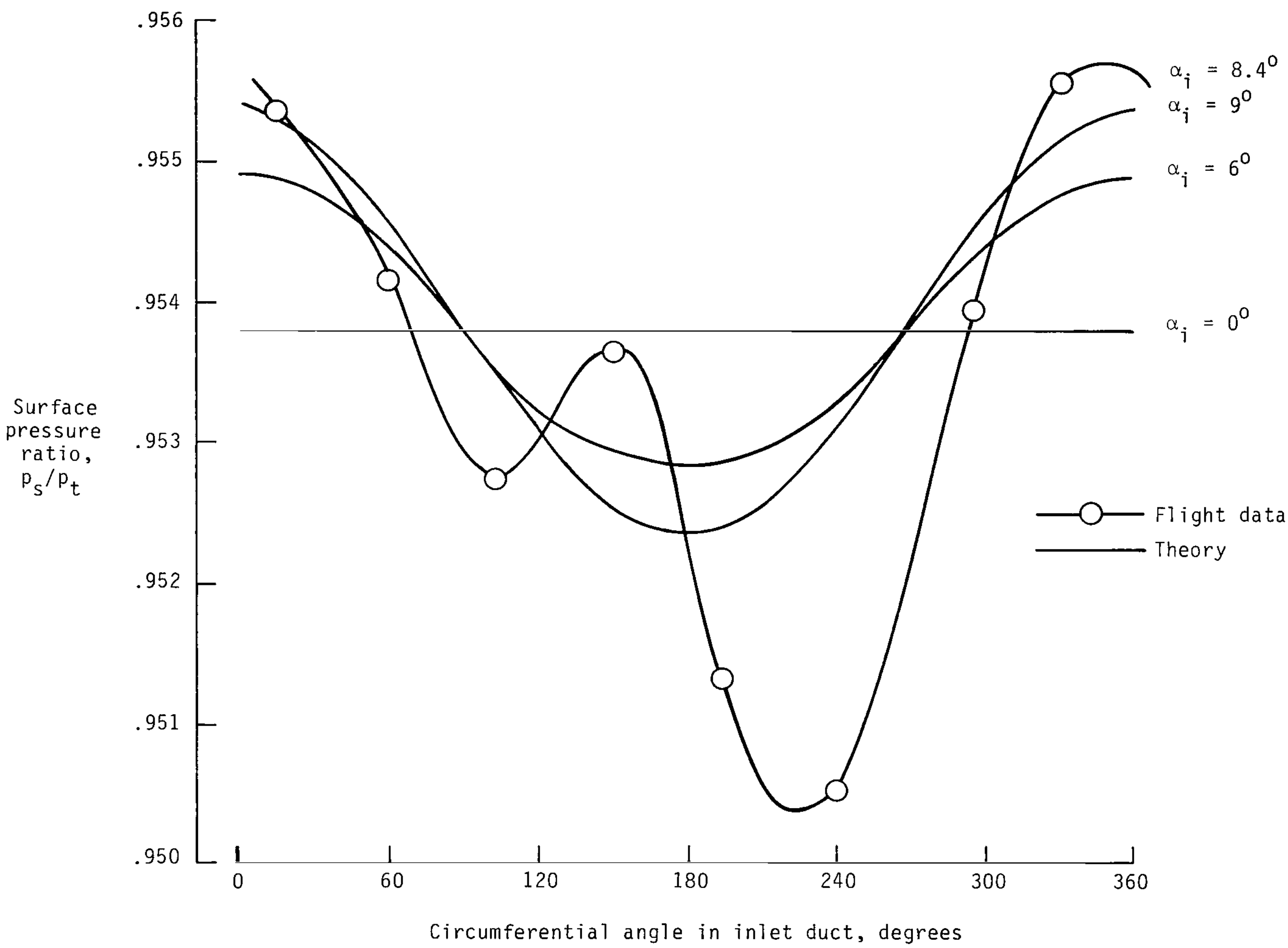

Figure 21.- Comparison of flight data with computer simulations of circumferential inlet pressure distributions at station 30.000 for various angles of attack.

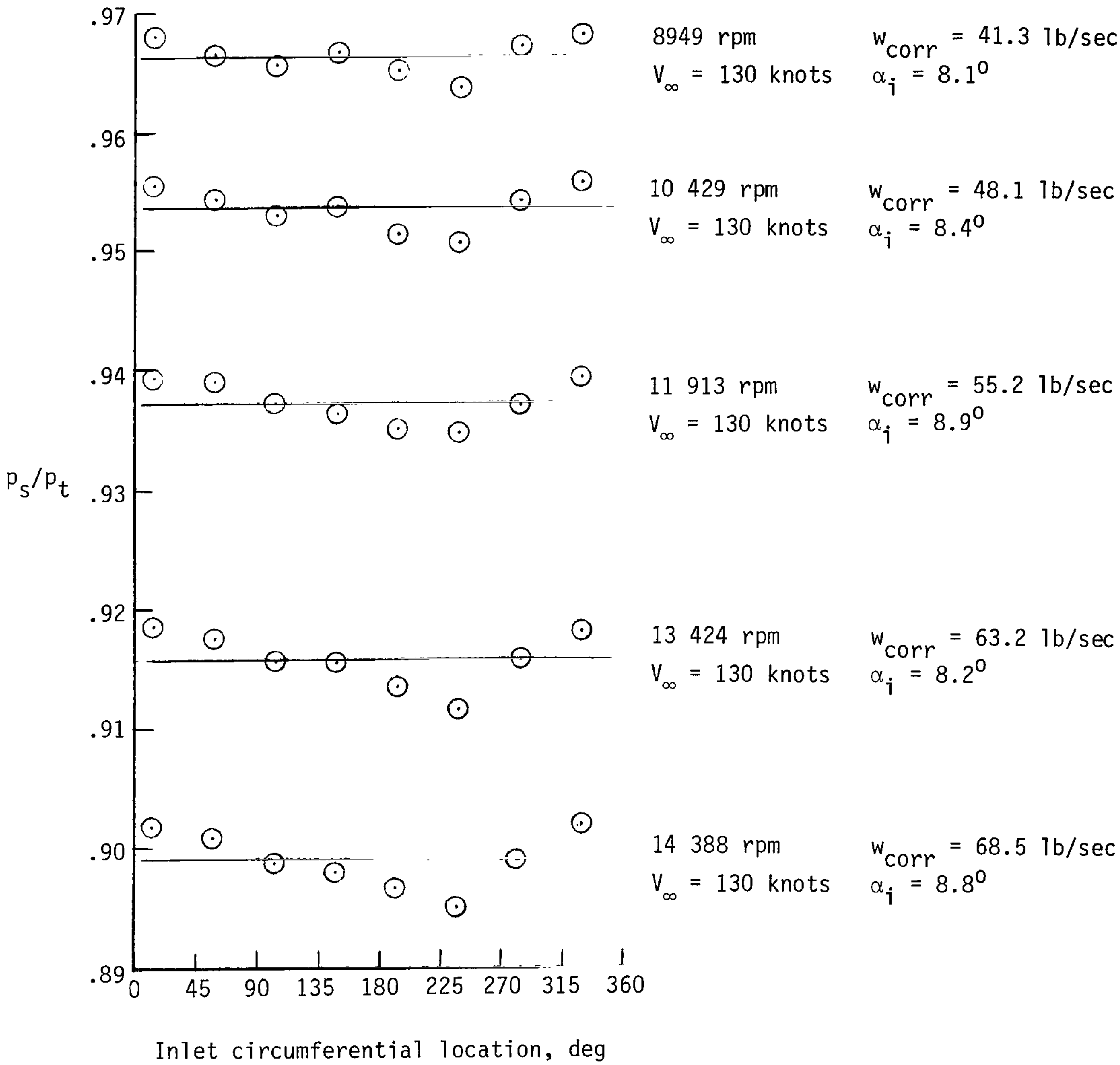

Figure 22.- Circumferential inlet pressure distributions at station 30 for various fan speed (N_1).

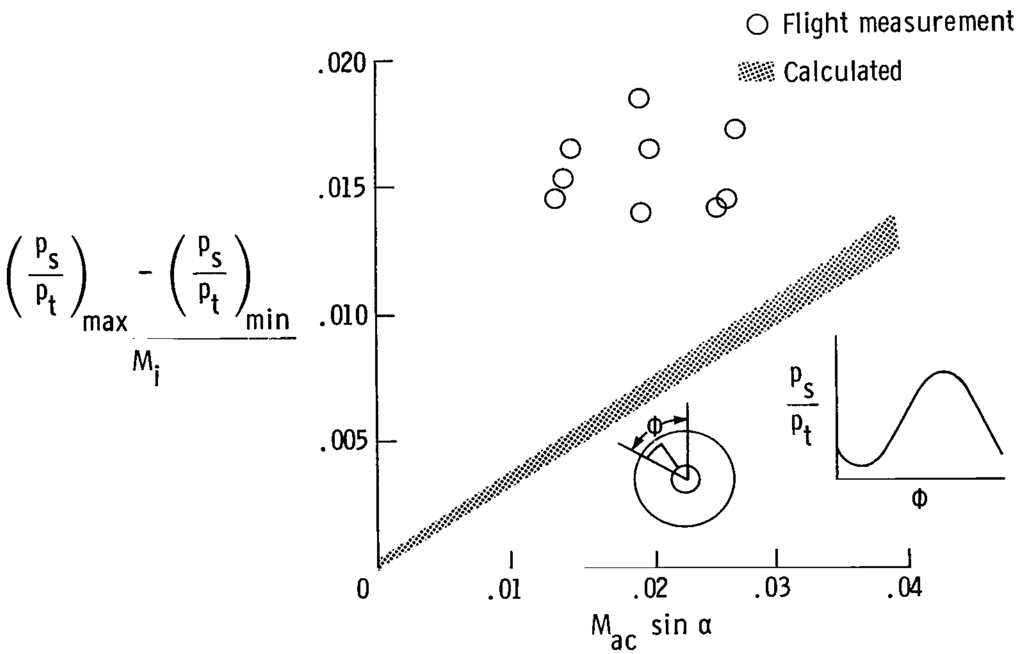

Figure 23.- Comparison of flight-measured and calculated inflow distortion at angle of attack.

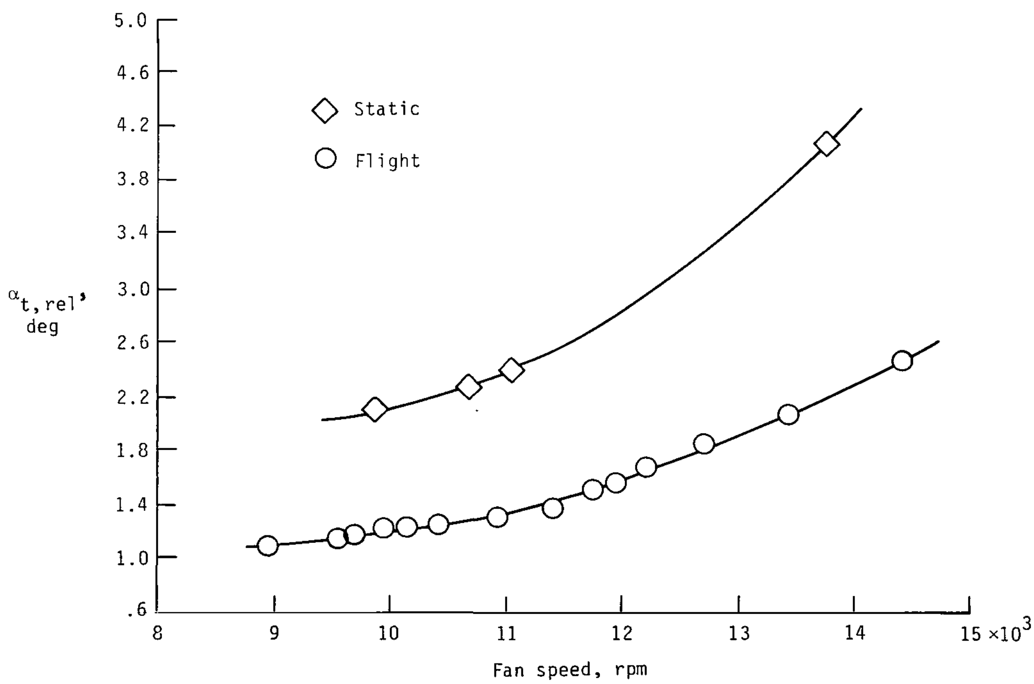

Figure 24.- Variation of $\alpha_{t,rel}$ with fan speed.

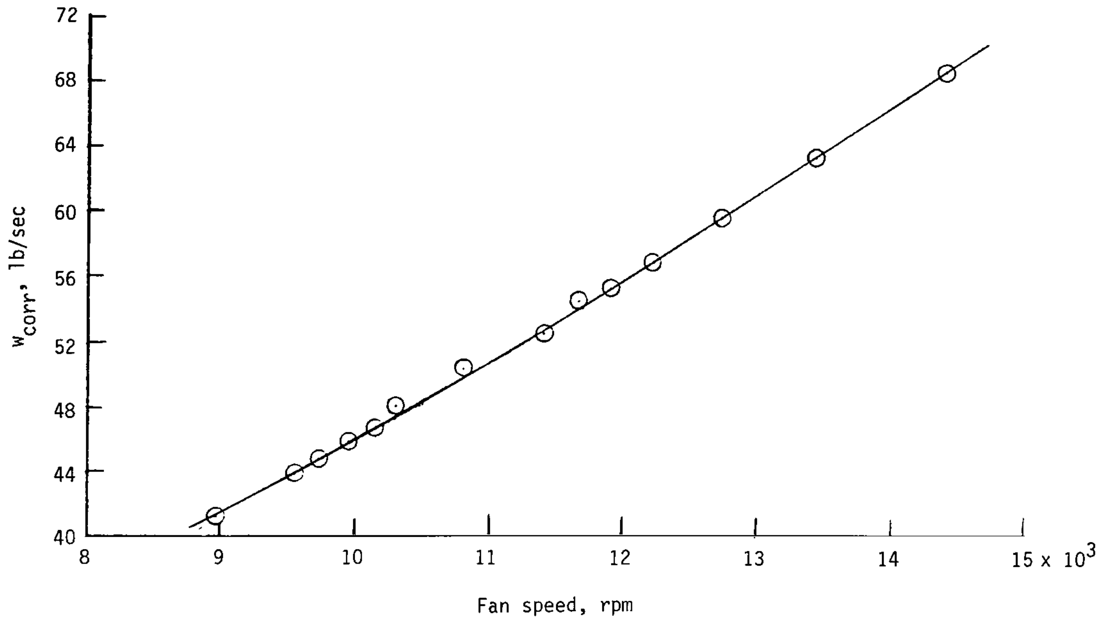

Figure 25.- Variation of corrected weight flow with fan speed.

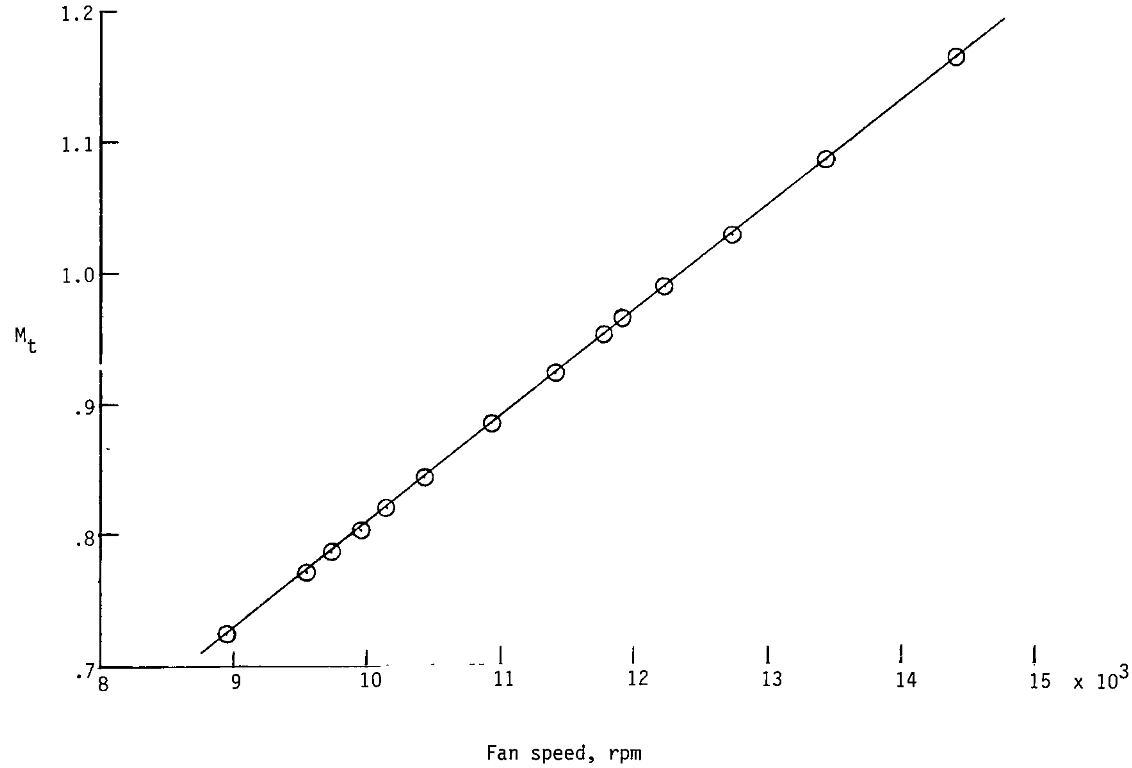

Figure 26.- Variation of Mach number of fan-blade tip with fan speed.

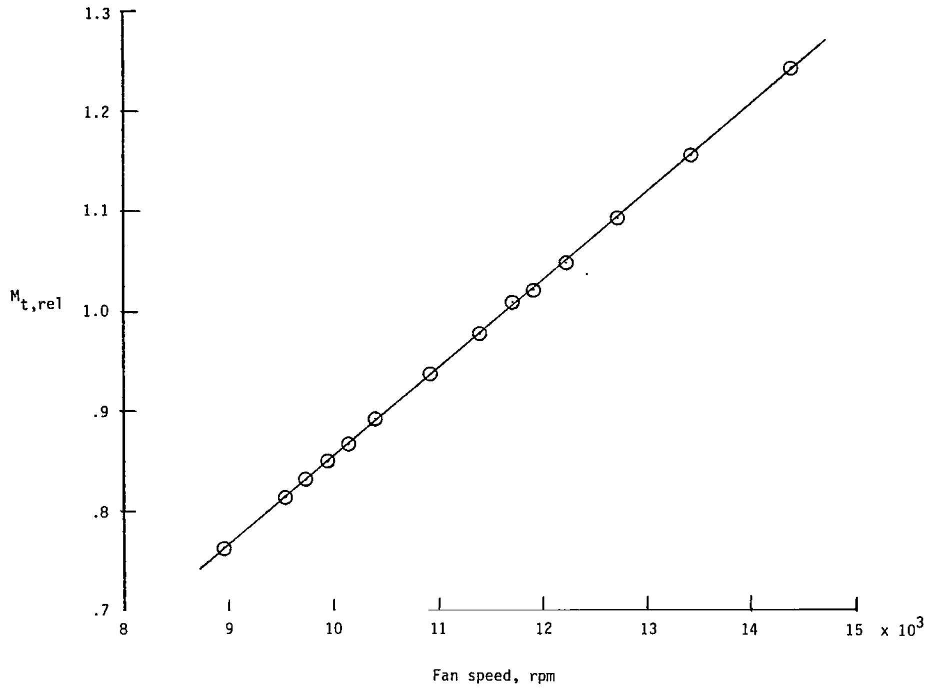

Figure 27.- Variation of relative Mach number of fan-blade tip with fan speed.

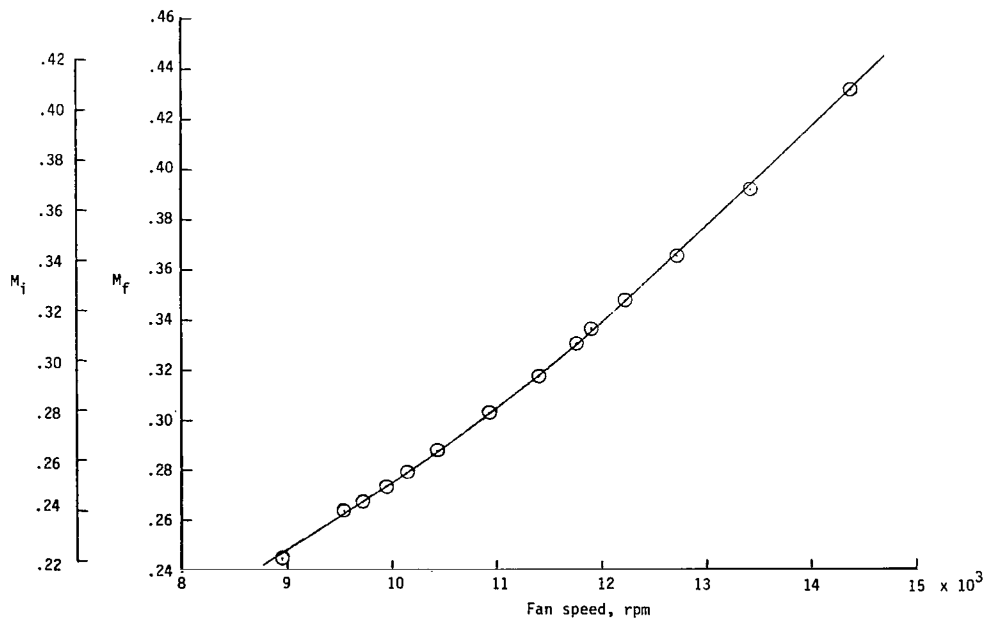

Figure 28.- Variation of inlet Mach number with fan speed.

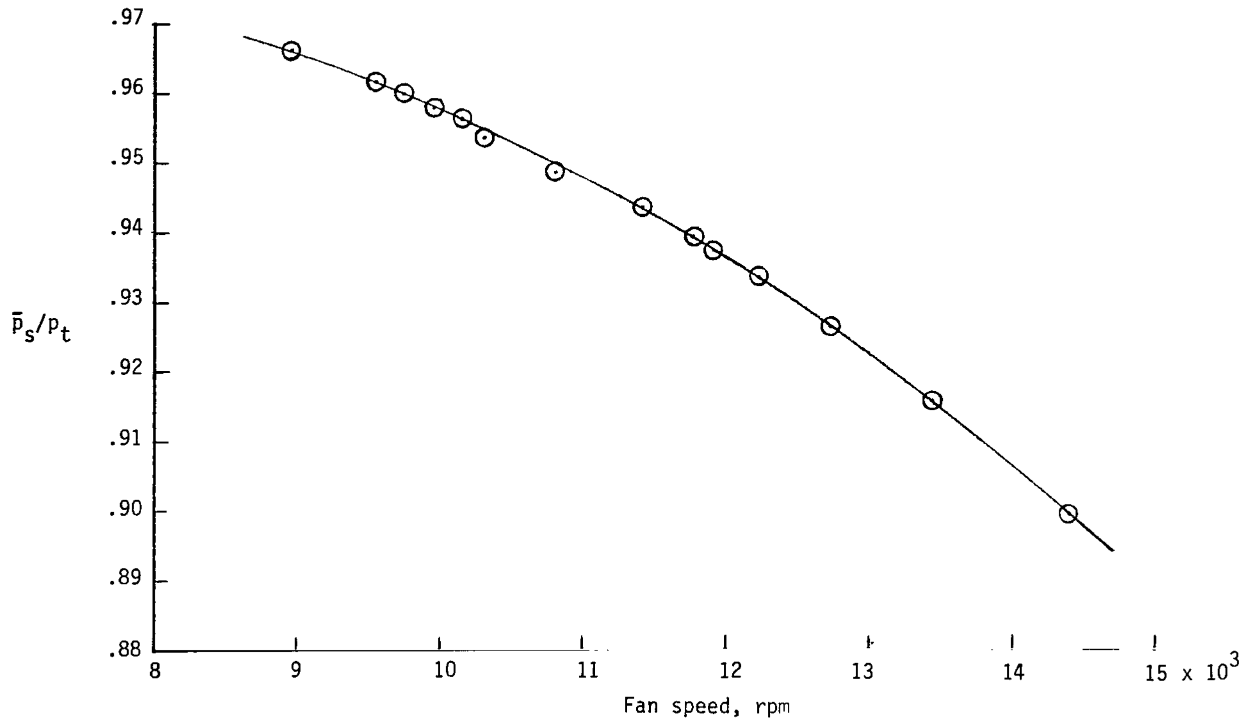

Figure 29.- Variation of inlet static-to-total pressure ratio with fan speed.

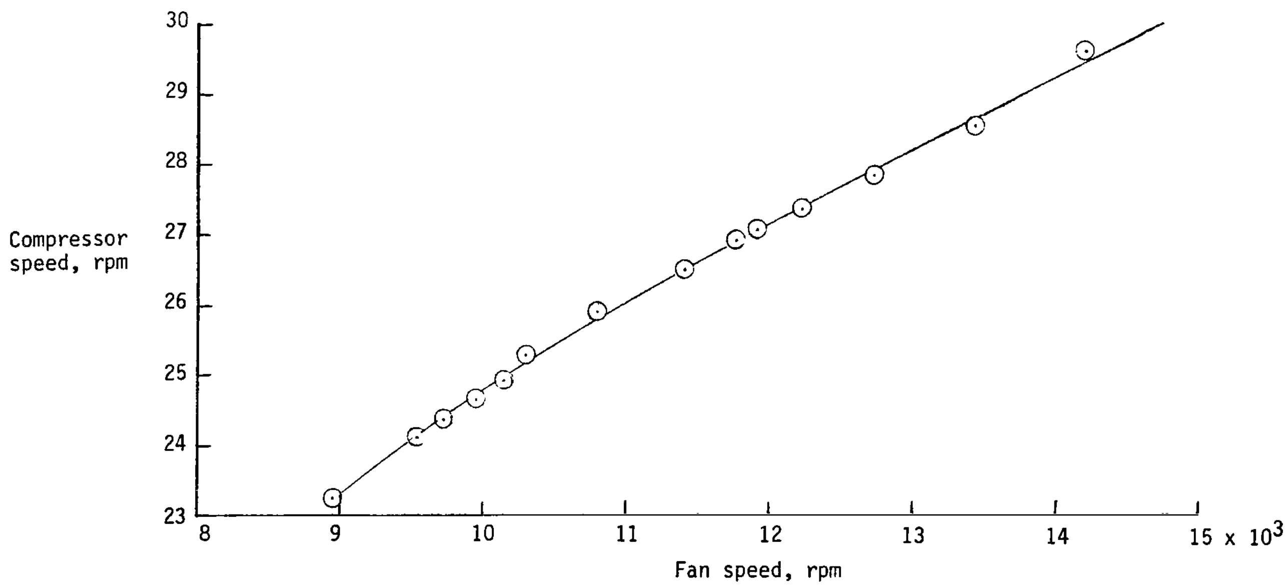

Figure 30.- Variation of compressor speed with fan speed.

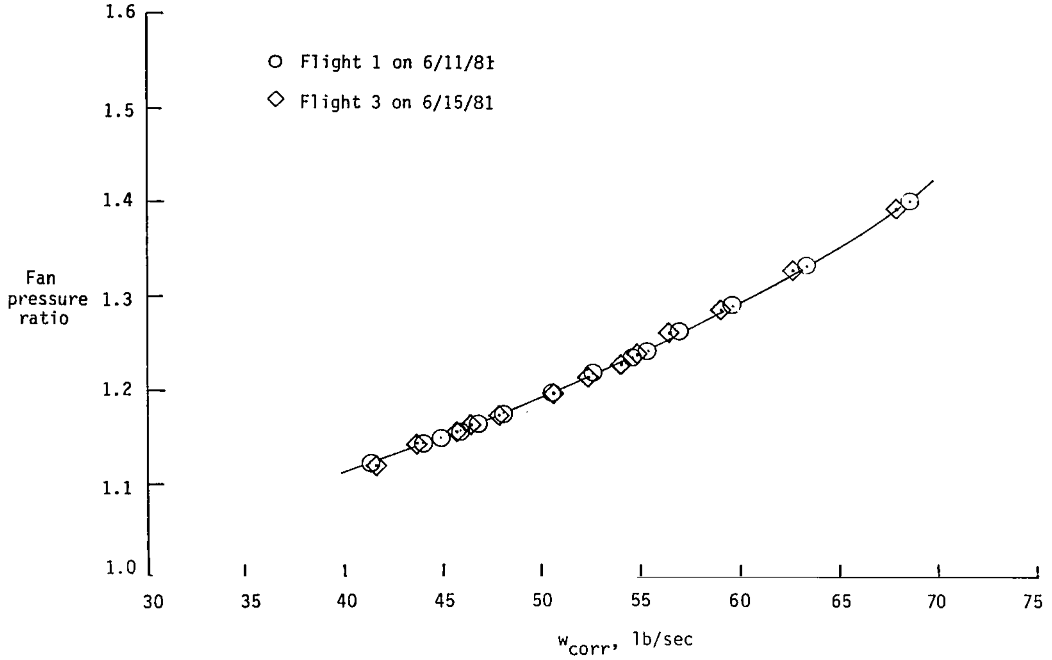

Figure 31.- Flight fan operating line comparison.

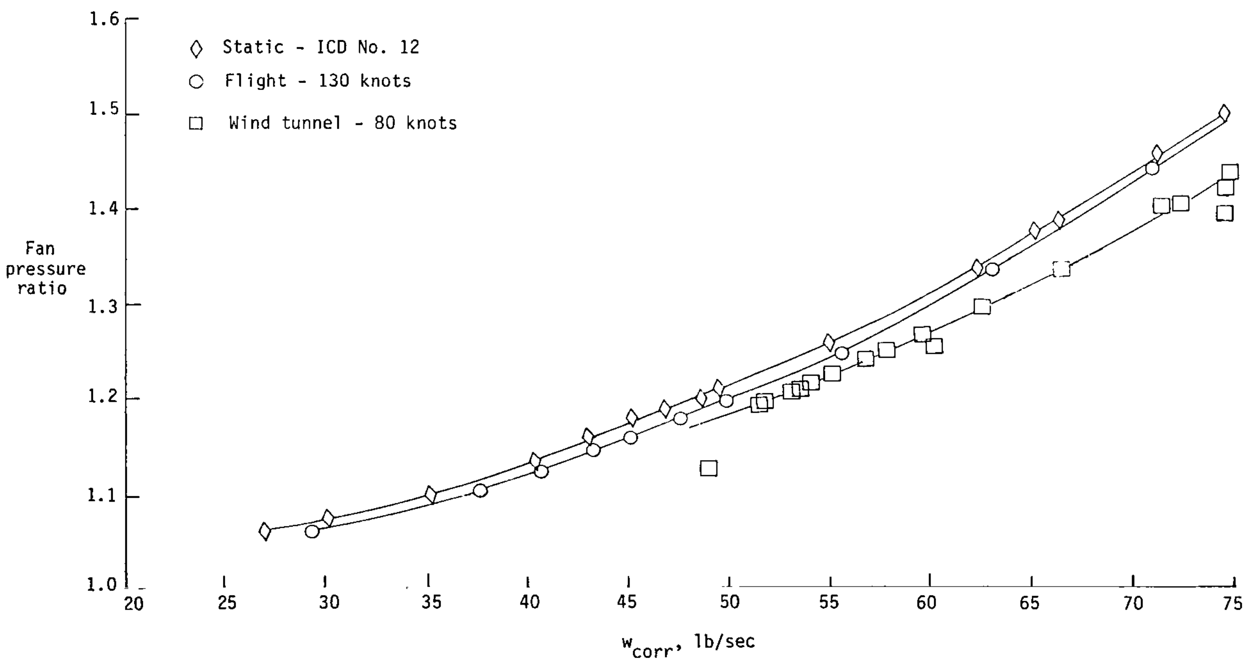

Figure 32.- Fan operating line comparison using flight research inlet and acoustic treatment for engine exhaust.

APPENDIX A

DETAILS OF AIRCRAFT-ENGINE MODIFICATIONS AND OPERATIONS

This appendix contains brief descriptions of (1) the details of the modifications to the Grumman OV-1B Mohawk aircraft to enable it to safely carry and support the operation of the Pratt & Whitney JT15D-1 engine, (2) the operation of the JT15D-1 engine with emphasis on the gas paths and rotary components, and (3) hardware modifications and instrumentation added to the JT15D-1 engine in order to carry out the fan-noise research program.

Aircraft Modification

A contract was awarded to the Grumman Aerospace Corporation (GAC) for the design, fabrication, assembly, and testing of modification to install a JT15D-1 turbofan engine on an OV-1B Mohawk aircraft. In the discourse which follows, only pertinent points of the OV-1B modifications and analysis are covered. A more detailed explanation can be found in the Grumman final report for this contract (ref. 27).

Structural analyses.- Structural analyses were performed by GAC on the proposed test-bed aircraft. The loads analysis included flight loads, landing loads, internal loads, and margins of safety required. Stress analyses were done on the hardback assembly, sway braces, bomb rack, pylon post, internal-wing pylon support structure, and wing structure. Fatigue life was investigated and determined not to be a problem for a research mission of up to 4 years with not more than 300 hours of operation. Flutter and divergence were also shown not to be a problem for the proposed research mission. Results of the structural analyses in terms of flight restrictions are as follows:

Maximum symmetric pull-up maneuvers, 2g acceleration

Maximum symmetric push-over maneuvers, 0g acceleration

Maximum bank angle of 30°

Landings and take-offs from smooth hard runways

Flared landings only to a maximum sink speed of 6 ft/sec

Maximum flight speed of 200 knots

No abrupt maneuvers

Maximum roll rate of 30° per second

Maximum allowable sideslip:
12° at 100 knots
7° at 150 knots
4° at 200 knots

No penetration of "moderate buffet"

300 flight hours in test configuration

APPENDIX A

Test engine fit to aircraft.- A production JT15D-1 engine was furnished to GAC by NASA to be used in place of the modified JT15D-1 in order to fit the engine to the aircraft. The production engine was also used for the flight testing of the modified aircraft. The engine was supplied with all the transducers and indicators required for normal JT15D-1 operation.

A solid aluminum hardback was designed and fabricated which bolted to the two top forward and one top aft JT15D-1 engine mounts (fig. A1). The forward engine mount takes fore, aft, vertical, and side loads. The aft engine mount needed only to take vertical and side loads. The hardback was designed to adapt to the normal OV-1B bomb rack and sway-brace support points at wing station 185. A special fitting was installed at the forward lug hook attachment point to prevent fore and aft movement of the package. The jettison capability at this stores station was disabled.

A Cessna Citation nacelle (model 550) was fitted to the engine. Because the 550 nacelle "side-mounts" on a rear fuselage, a new left-side upper cowl was fabricated, and the nacelle was then modified to the required vertical support from the OV-1B wing.

Internal wing changes.- The deicer boot and the wing leading-edge panels were removed from the right wing (fig. A1). This gave wing access to install the necessary JT15D-1 engine control lines and electrical wires, research instrumentation wires, fuel lines, and fire extinguisher lines. The existing fuel feed line, which transfers fuel from the right drop tank to the main tank, was used to route fuel to the JT15D-1 by simply reversing the direction of the pumping action of the wing tank transfer pump. A vent fuel line was then added in the leading wing edge which vented the engine fuel system back into the main tank. The wing leading-edge and deicer boot was replaced after completion of the aforementioned work.

JT15D-1 controls and instrumentation.- Figure A2 is a forward view of the test-aircraft cockpit arrangement. The JT15D-1 engine monitoring instruments were installed in the observers instrumentation panel. The readouts included fan speed N_1, compressor speed N_2, interturbine temperature (ITT), engine oil pressure, and engine oil temperature. The JT15D-1 engine vibration levels were measured and recorded during flight but were not displayed. A red warning light in the cockpit was used to indicate that the engine vibration levels were beyond a preset limit. The engine would be shut down immediately if the red light illuminated. A quadrant throttle control for the JT15D-1 engine was installed on the right side of the upper-center control console adjacent to the throttle controls for the two turboprop engines. The JT15D-1 engine power, fuel, and start switches were installed in the lower-center control console so that they were easily accessible by the pilot and observer.

Nose-boom mounting provisions.- GAC fabricated and installed structural provisions for an instrumentation boom in the fuselage nose of the aircraft. This included modifications to the aircraft nose cap and structural reinforcement of the primary nose structure to carry the nose-boom loads.

Modified aircraft flight test.- The contractor was required to define and execute a flight-test program to satisfactorily demonstrate operation of the aircraft, its subsystems, and modifications made during the contract. The flight testing included the significant extremes of the aircraft envelope that were measurable with cockpit instrumentation.

APPENDIX A

Engine Description and Modifications

The test engine was a JT15D-1 turbofan engine manufactured by Pratt & Whitney Aircraft of Canada. The engine is a twin-spool, front-fan, jet-propulsion engine which has a full-length annular bypass duct. It has a nominal bypass ratio of 3.3 and a maximum thrust capability of 2200 lb. (See table A1 for design features.) Figure A3 is a front and rear side view of a production JT15D-1 engine.

Figure A4 is a schematic which shows the rotating blades, stator vanes, and structural components of the engine. Air entering the engine first encounters the 21-in-diameter fan, which has 28 blades. (See figs. A3 and A4.) Behind the fan is a stator assembly (fig. A5), which separates the airflow into a bypass-duct flow and core-duct flow. The bypass stator consists of 66 split vanes which reduce circumferential air motion to a very slow swirl. The bypass air then passes by the six engine support struts (fig. A6), and, after traveling the full length of the bypass duct, exits through a bypass nozzle whose exit is not normally coplanar with the core flow. About three-fourths of the total thrust is produced by the bypass air flow. Any noise produced in the inlet or by interaction between the rotating fan and any stator vanes or structural engine components is free to propagate either forward out of the inlet or aft out of the bypass-duct exhaust. Therefore, it was necessary that test data collected from the ground, wind-tunnel, and flight testing which was to be compared have acoustic treatment for the bypass-duct exhaust during the testing. The core stator of a production engine has 33 blades and guides the air past 6 internal support struts (fig. A6) and into the compressor. The compressor is a combination axial-centrifugal type which has 16 full-length blades and 16 splitter blades. The core airflow then passes into the diffuser section and subsequently into the reverse annular burner, where it is mixed with the fuel for combustion. After combustion, the core-exhaust gases pass through a series of power turbines (each separated by a stator-vane assembly). The first turbine provides power to drive the compressor, and the next two stages drive the fan. The exhaust gases then exit through the core nozzle. The core flow provides approximately one-fourth of the total engine thrust.

The modifications to all the JT15D-1 engines used in this program were performed by Pratt & Whitney Aircraft (PWA). The instrumentation system furnished by PWA provided a means for measuring and/or monitoring the inlet-generated noise and fan performance. The dynamic instrumentation measurement system consisted of fan-blade and stator-vane transducer measurements. Figure A7 shows the blade-mounted transducer instrumentation system (BMTIS) hardware installed in the JT15D-1 flight engine. Figure A8 is an electrical schematic of the BMTIS, which shows that the rotating-blade transducer signals are telemetered (via the modified nose-cone electronics) to a receiving antenna in the nacelle inlet wall. These signals are amplified and routed, along with a once per revolution signal and a time code, to the aircraft instrumentation tape recorders. This system is described in detail in reference 18. Some measurement results are presented in reference 28.

PWA also installed structural provisions for mounting three NASA furnished pressure-temperature rake assemblies in the JT15D-1 engine bypass duct (fig. A7). Each of the rake assemblies contains six total-pressure tubes and five thermocouples, which are positioned radially across the annular bypass duct and approximately 120° apart circumferentially. Readings from each of the three locations are averaged to yield the bypass-duct total pressure and temperature. There is an additional port for measuring the static pressures at each of the rake assemblies.

A modified stator assembly (see fig. A9) was also designed and fabricated by PWA. A production core stator has 33 vanes, but the modified core stator contains

71 vanes. In addition to increasing the number of blades, the distance between the fan-rotor core and the core-stator assembly was increased by 123 percent (fig. A10). By increasing the spacing and number of stators, the fan-rotor/core-stator tone was acoustically cut off and the broadband noise was diminished.

TABLE A1.- JT15D-1 DESIGN FEATURES

Take-off rating thrust, lb	2200
Maximum fan speed, N_1, rpm	16 000
Maximum compressor speed, N_2, rpm	32 000
Maximum bypass ratio	3.3
Maximum fan pressure ratio	1.5
Rotor diameter, in.	21
Ratio of hub to rotor tip	0.4
Number of rotor blades	28
Number of bypass-stator vanes	66
Number of core-stator vanes[a]	71
Bypass rotor-stator spacing	1.83
Core rotor-stator spacing[b]	0.63

[a]Production engine has 33 core-stator vanes.
[b]Production engine core rotor-stator spacing is 0.28.

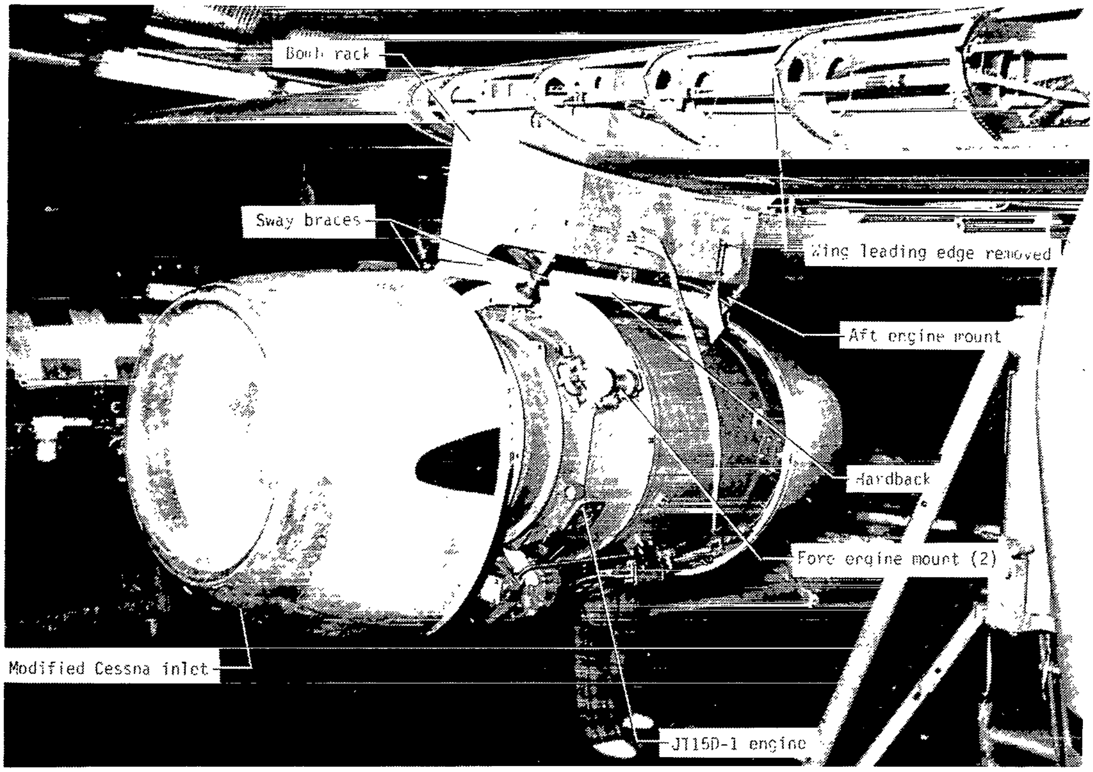

Figure A1.- JT15D-1/OV-1B structural modifications.

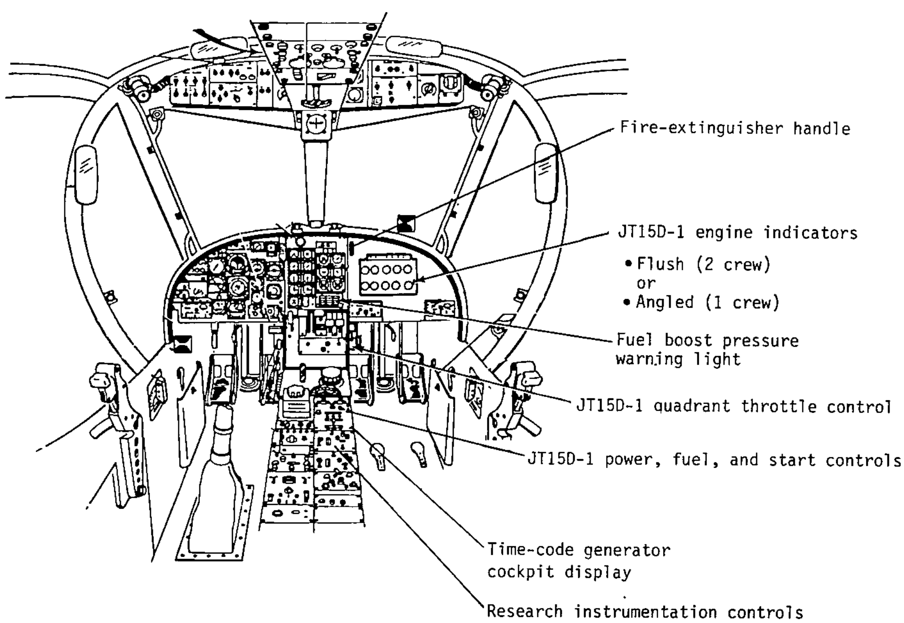

Figure A2.- Test-aircraft cockpit arrangement.

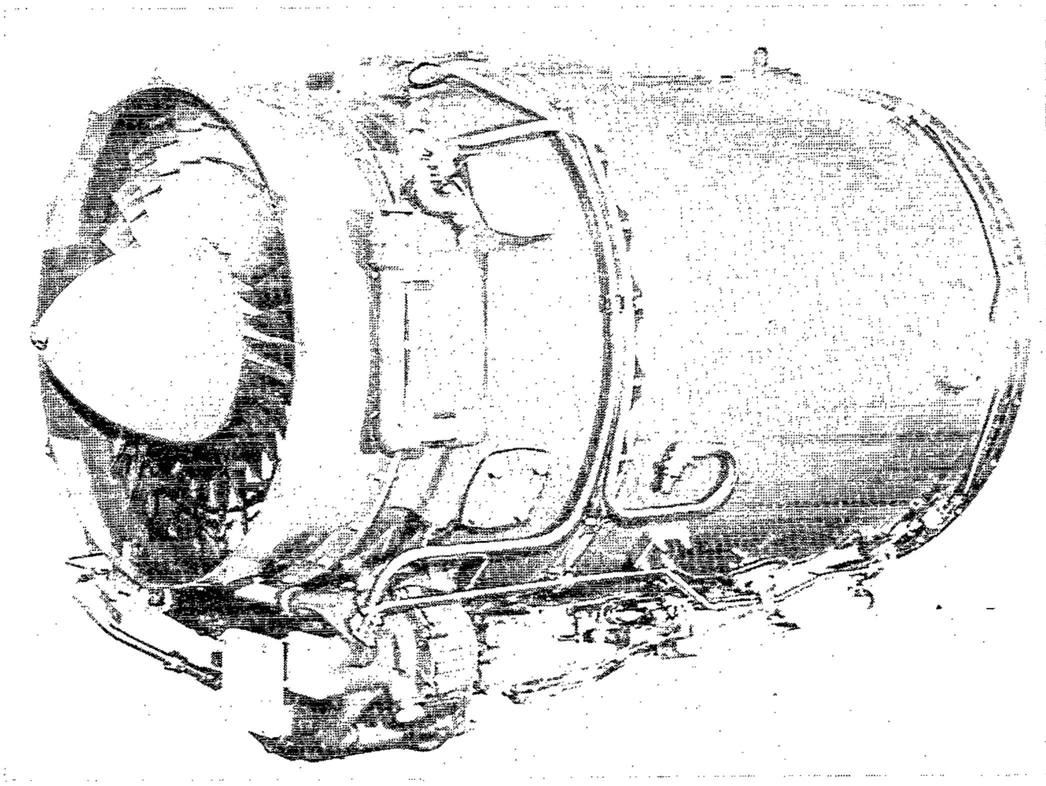

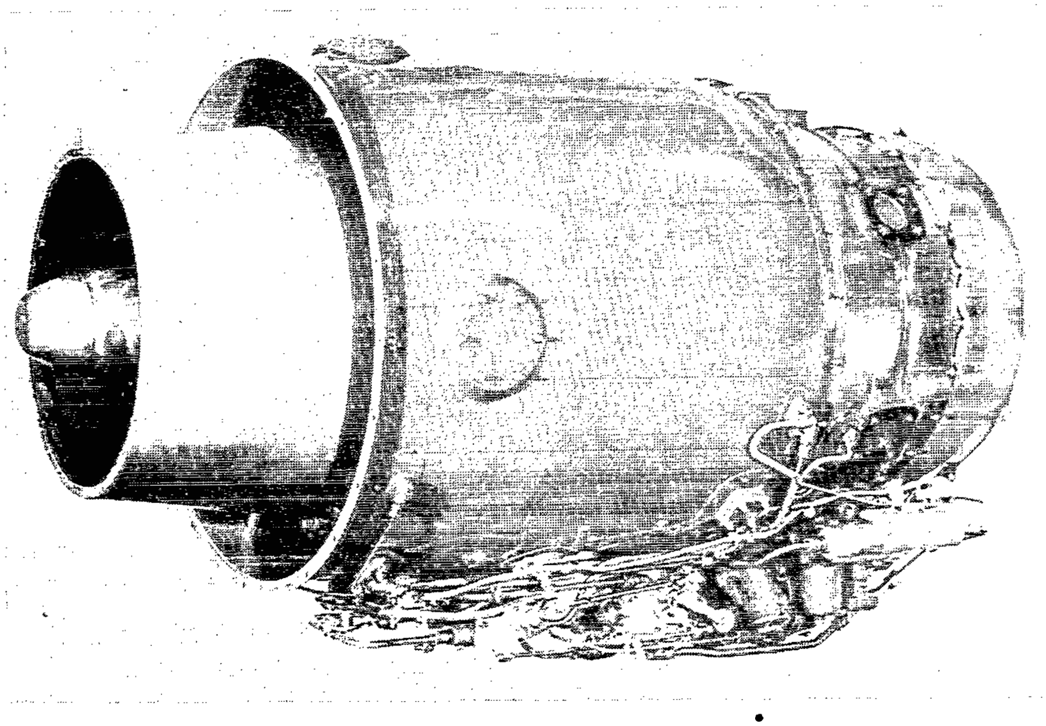

Figure A3.- JT15D-1 production engine.

Stations

1 Ambient
2 Engine inlet
2.4 ID Low compressor (inner discharge)
2.4 OD Low compressor (outer discharge)
2.5 High-compressor inlet
2.6 Bypass-duct static
3 Burner inlet
4 High-compressor turbine inlet
5 Low-compressor turbine inlet
6 Exhaust duct
7 Pickup plane for airframe-supplied jet nozzle

Rotating vanes
Stationary vanes

Flanges

A Low compressor case to intermediate case
B Intermediate case to bypass duct
C Gas generator to low turbine stator
D Low turbine stator support to exhaust

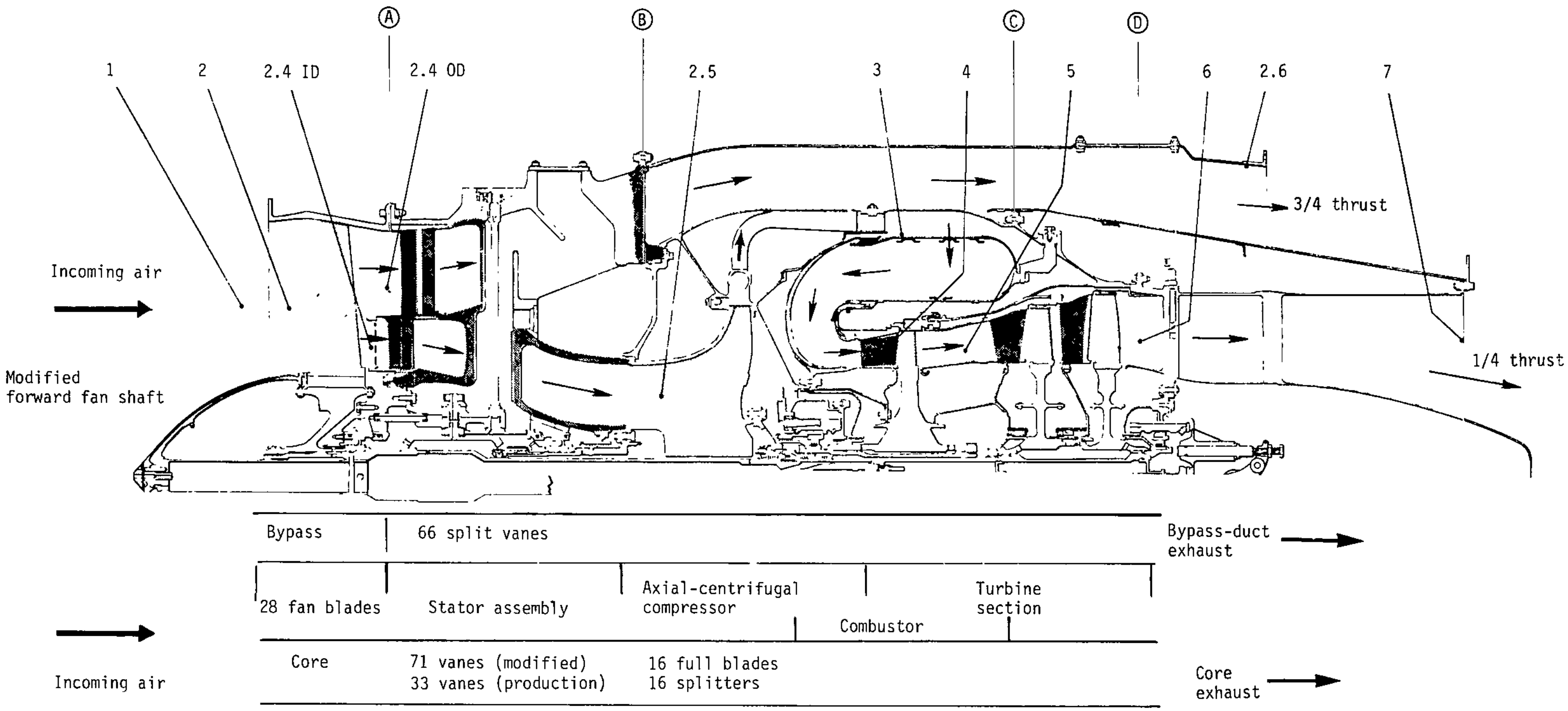

Figure A4.- JT15D-1 airflow and blade schemetic.

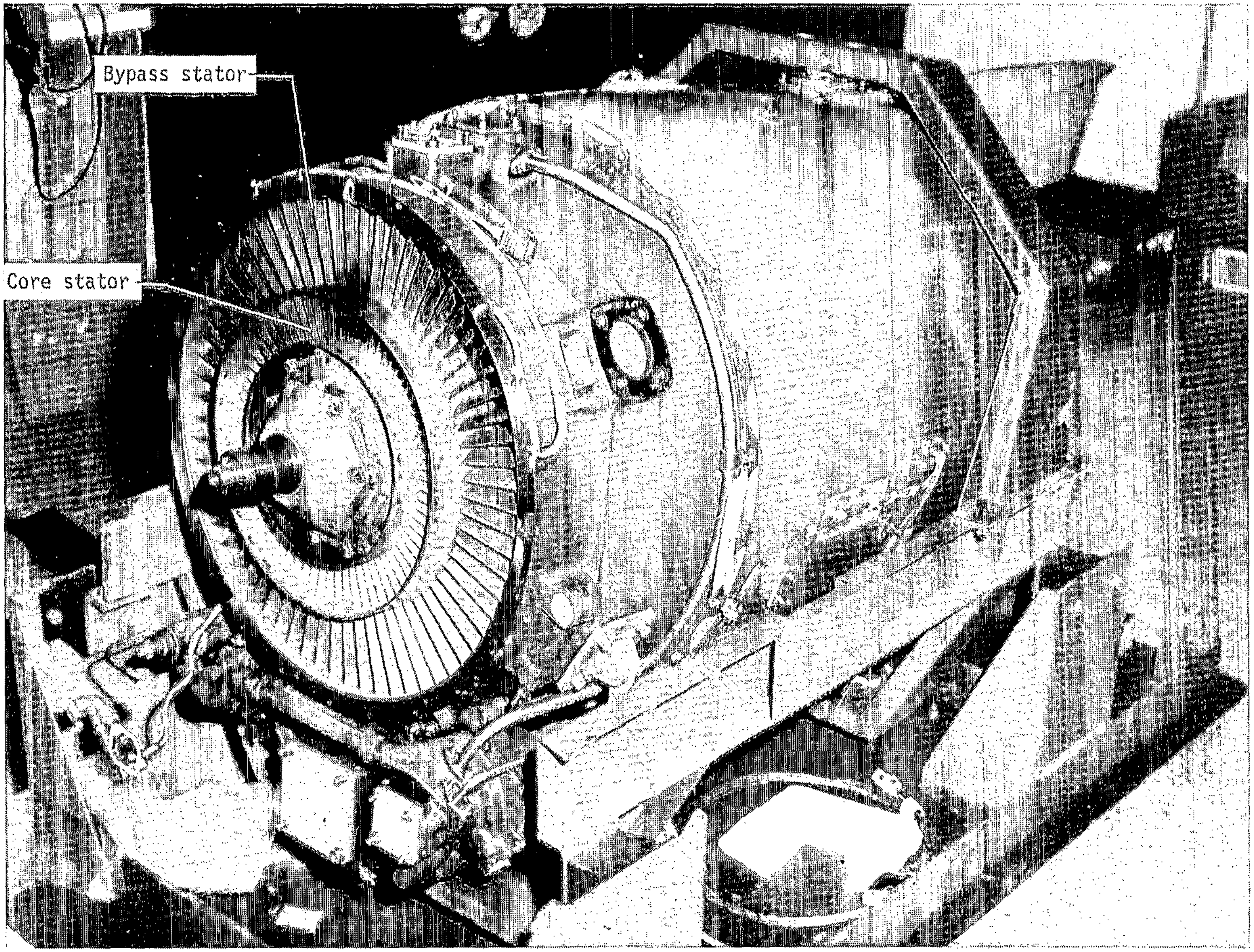

L-80-899.1

Figure A5.- View of JT15D-1 showing stator assembly. Nose cone, fan case, and fan-blade assembly removed.

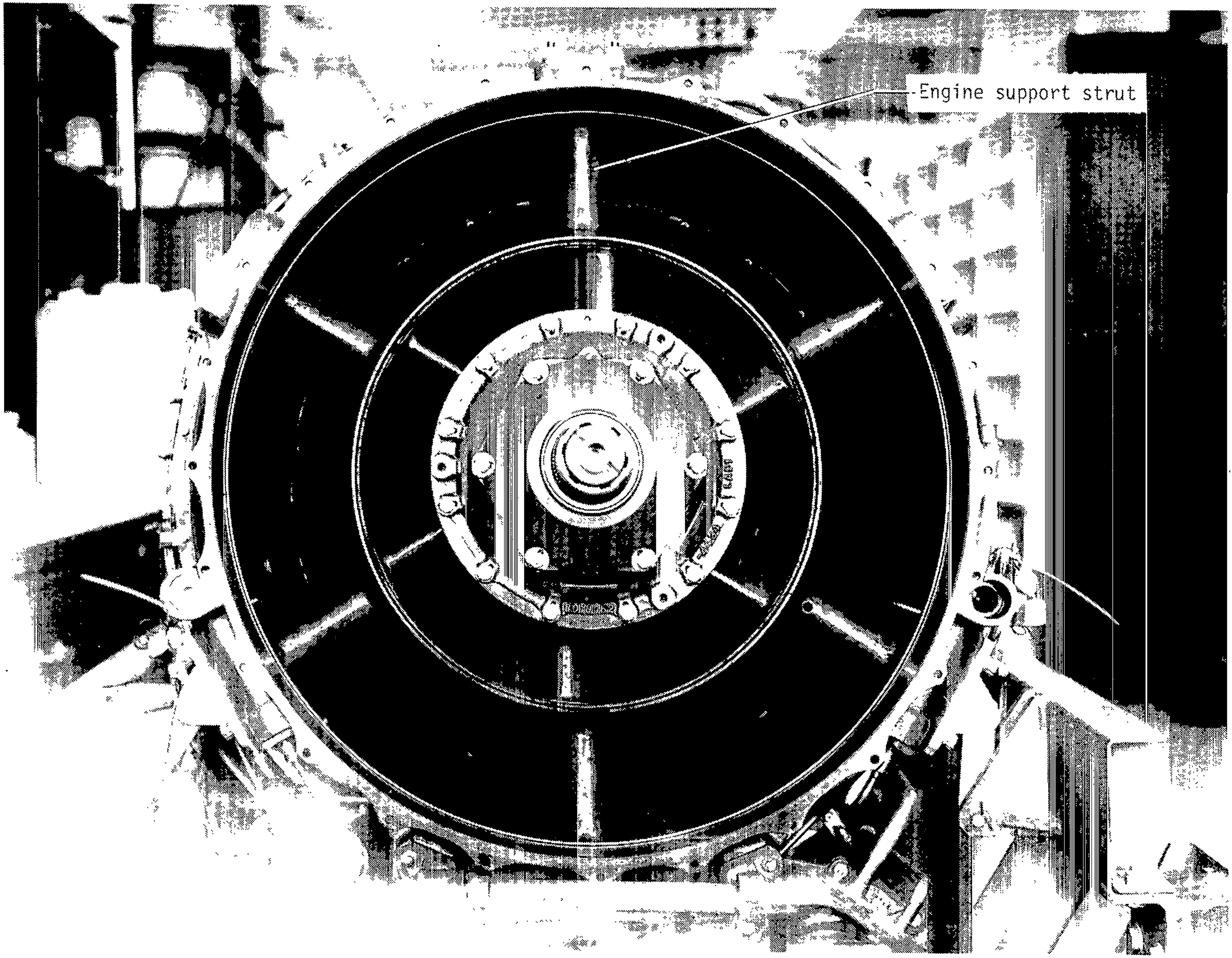

L-80-4221.1

Figure A6.- View of JT15D-1 showing engine support struts. Nose cone, fan case, fan-blade assembly, and stator assembly removed.

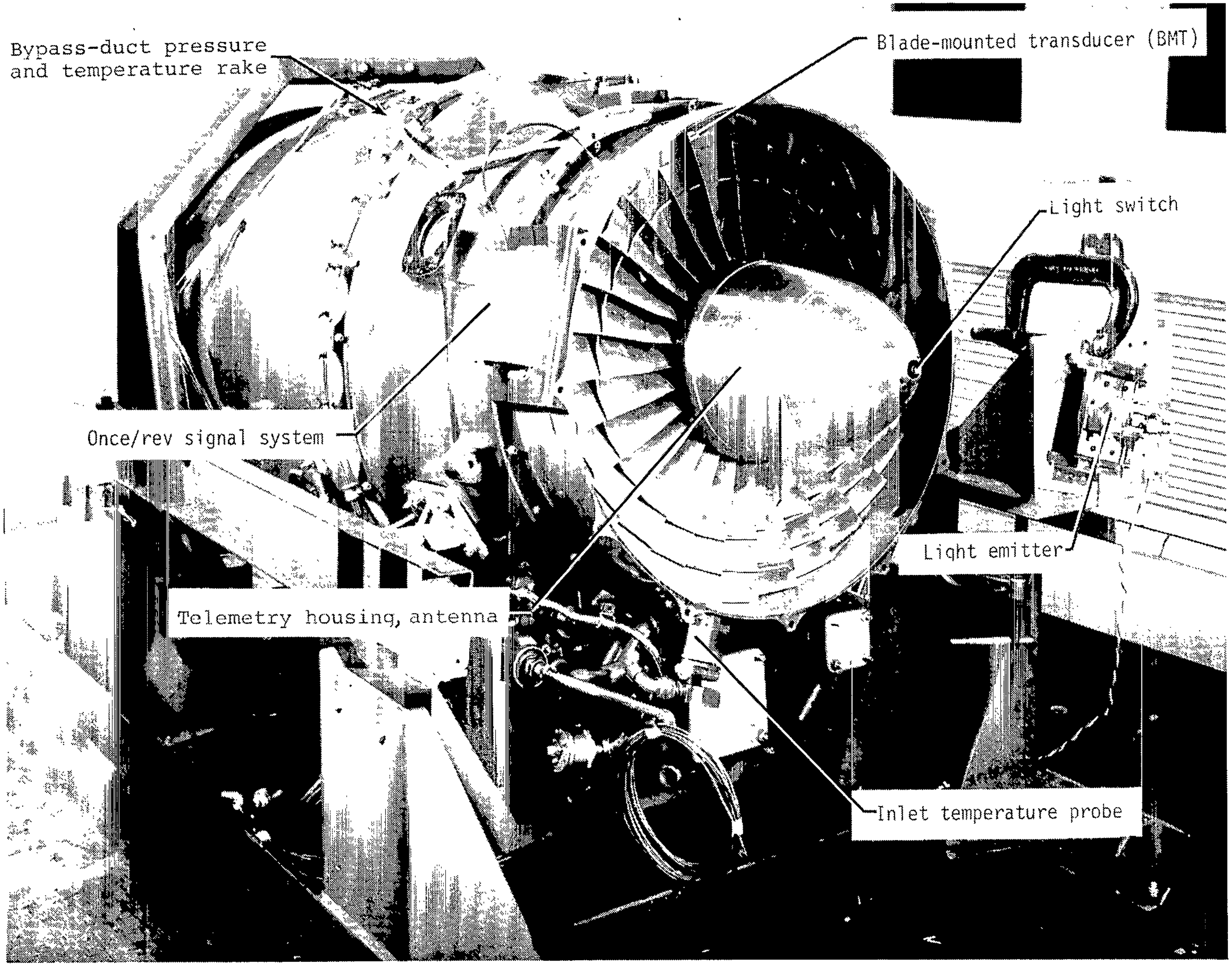

L-80-951.1

Figure A7.- JT15D-1 engine with blade-mounted transducer instrumentation system (BMTIS) installed.

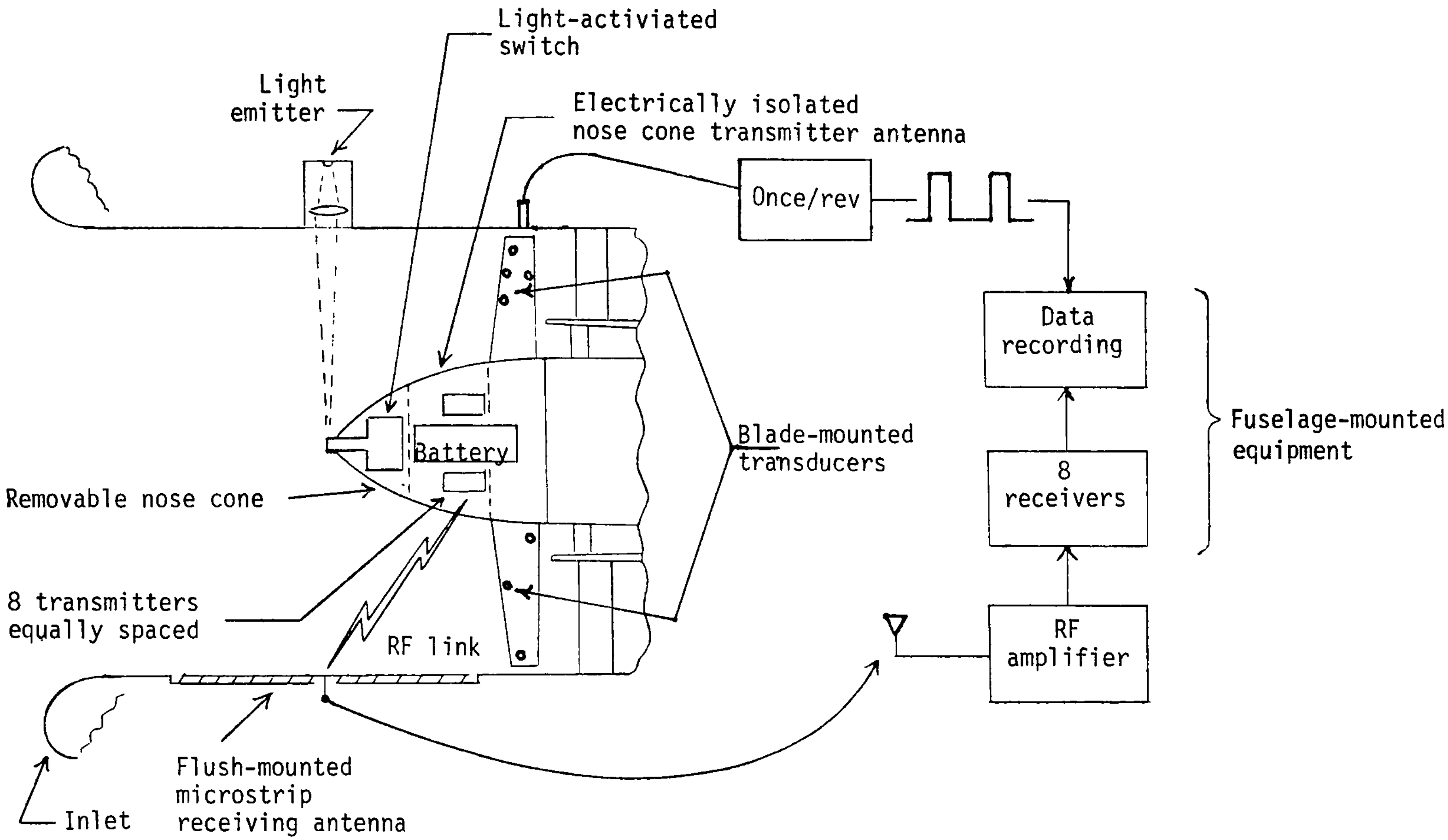

Figure A8.- Schematic of BMTIS.

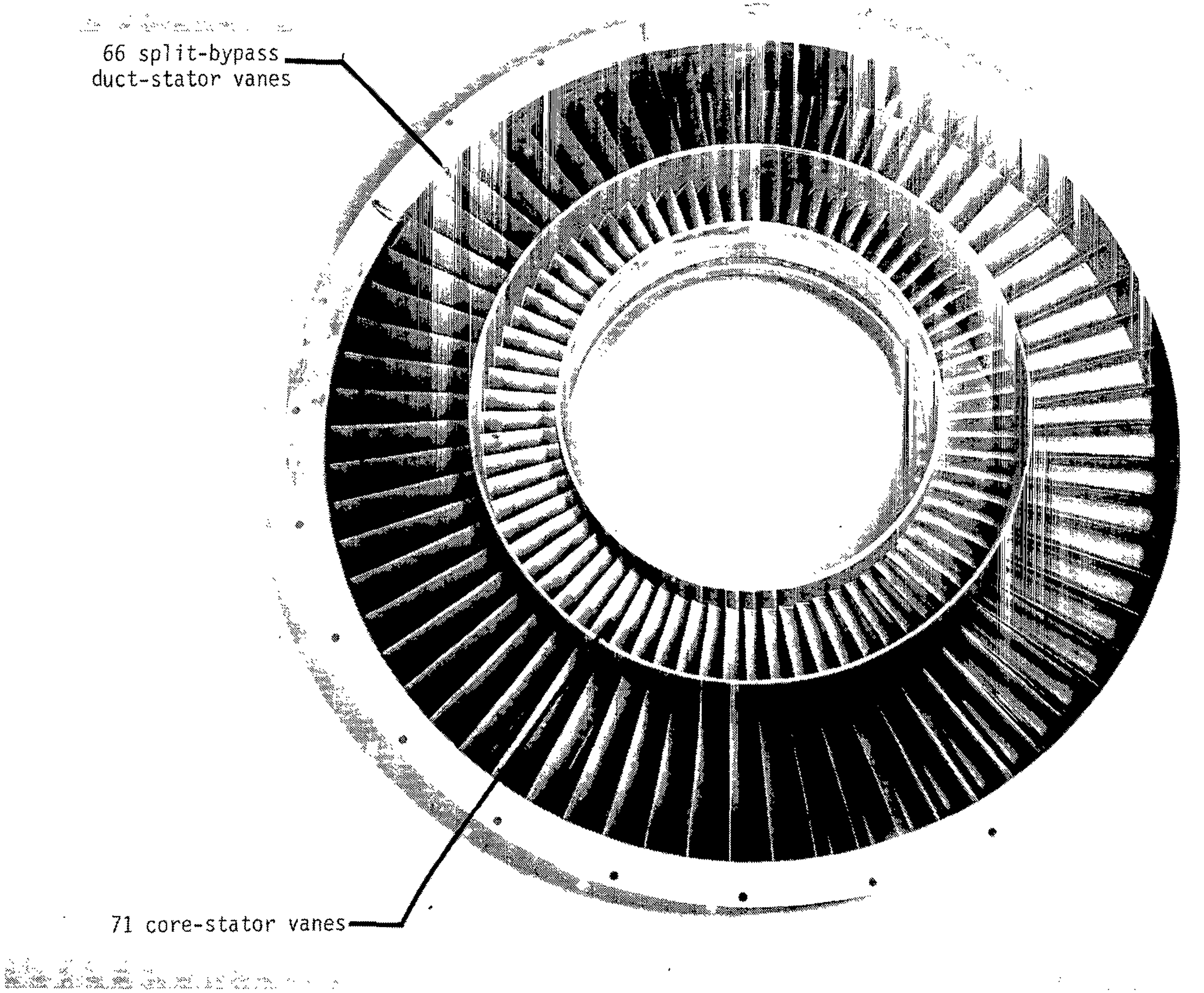

Figure A9.- Modified stator assembly for JT15D-1 engine.

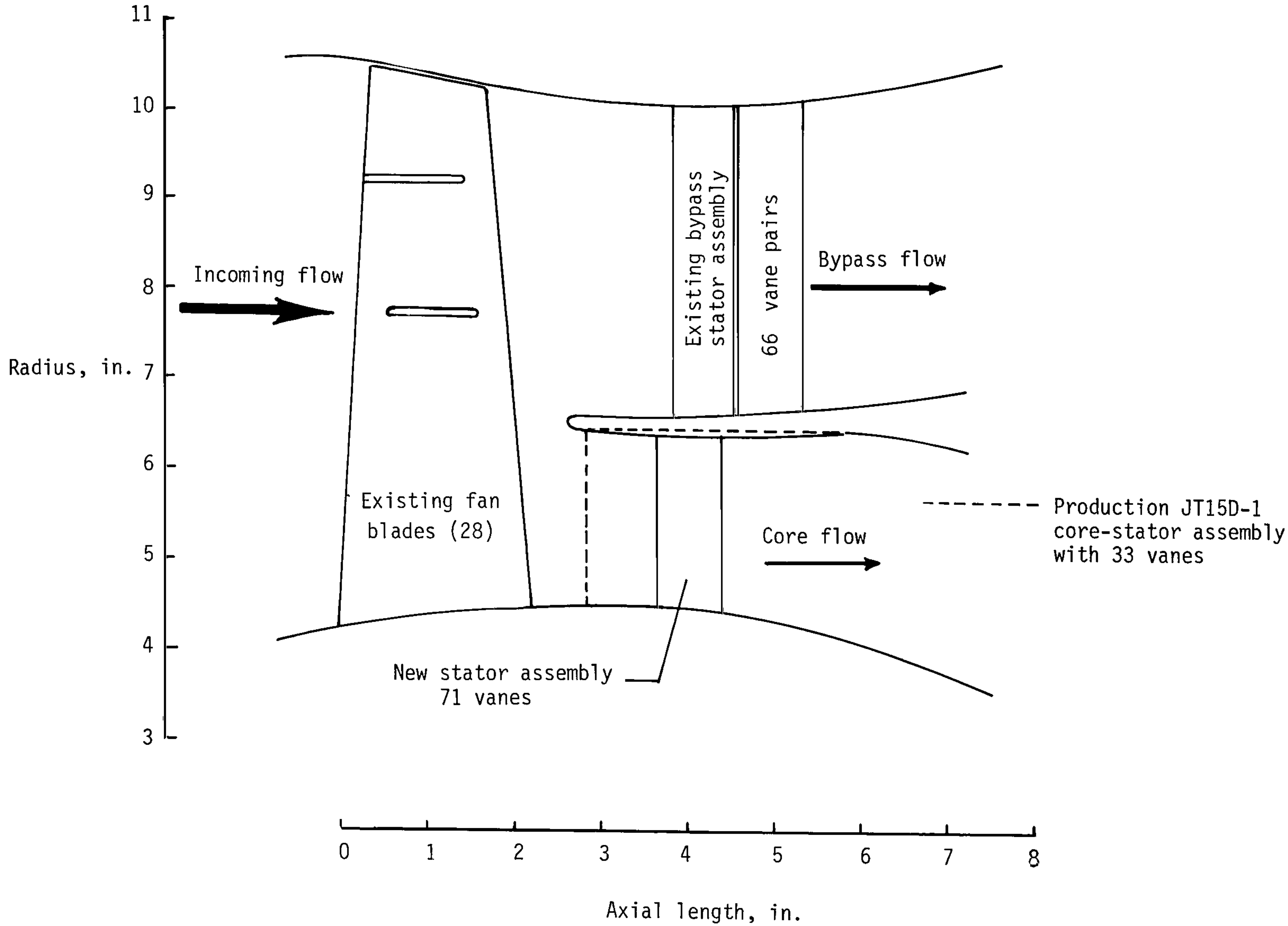

Figure A10.- Core-stator axial modification.

APPENDIX B

INLET AND ENGINE PERFORMANCE EQUATIONS

The pulse-code-modulated (PCM) data described in the body of this report were used to calculate the following inlet and engine performance parameters.

The speed of sound in the inlet duct c_i was calculated using the inlet temperature T_i as follows:

$$c_i = \sqrt{\gamma \frac{p_i}{\rho_i}} \approx 49.03\sqrt{T_i}$$

where T_i is in degrees Rankine and c_i is in feet per second.

The Mach number at the fan-blade tip is

$$M_t = \frac{\pi d_f N_1}{60 c_i}$$

where d_f is the duct diameter in feet at the fan face and N_1 is the fan speed in rpm.

The Mach number in the inlet duct at station 30 was obtained from the average of eight static-pressure measurements p_s at that station and total pressure $p_{t,i}$ obtained from the aircraft-boom pitot tube. Assuming isentropic compressible flow, then

$$M_i = \left\{\frac{2}{\gamma - 1}\left[\left(\frac{p_{t,i}}{p_{s,i}}\right)^{\frac{\gamma-1}{\gamma}} - 1\right]\right\}^{1/2}$$

The Mach number at the fan face was estimated from the relation

$$M_f = M_i\left(\frac{d_i}{d_f}\right)^2$$

The tip relative Mach number was determined from the vector sum of M_t and M_f as follows:

$$M_{t,rel} = \sqrt{M_t^2 + M_f^2}$$

A relative flow angle at the fan-blade tip was obtained from the difference between the geometric angle of the blade-tip chord (≈72°) and the flow angle as follows:

$$\alpha_{t,rel} = 72.0° - \arctan(M_t/M_f)$$

Fan pressure ratio is expressed as the ratio of inlet total pressure to bypass total pressure as follows:

$$FPR = \frac{p_{t,bp}}{p_{t,i}}$$

where the bypass total pressure was obtained by averaging readings from three pressure rates located in the bypass duct.

Inlet weight flow in pounds per second is given by

$$w = 36p_{t,i}\pi d_i^2 M_i \sqrt{\frac{\gamma g}{RT_{t,i}}}\left(1 + \frac{\gamma - 1}{2} M^2\right)^{-\left[\frac{\gamma+1}{2(\gamma-1)}\right]}$$

and corrected weight flow is given by

$$w_{corr} = \frac{w\sqrt{\theta}}{\delta}$$

where

$$\theta = \frac{T_{t,i}}{T_o}$$

and

$$\delta = \frac{p_{t,i}}{p_o}$$

Corrected fan speed is given by

$$N_{1,corr} = \frac{N_1}{\sqrt{\theta}}$$

APPENDIX C

SAMPLE PCM LISTING

The pulse-code-modulated (PCM) data listing (table C2) from the aircraft digital subsystem was used to evaluate inlet performance and to calculate engine performance parameters. Table C2 is a sample of the engineering units output and the subsequent calculated aircraft and engine performance parameters. These data, as shown on the first page of table C2, are from run 1043 flown on June 11, 1981, and correspond to a 27-second data recording period during which the aircraft flew over the microphone array.

After the completion of a flight test, consisting of a series of runs, the encoded data from tape recorder 2 containing the PCM channel were submitted to the Analysis and Computation Division at Langley Research Center. A computer program decoded the data tape, digitized the data, and, using the transducer calibration data and preflight calibration data, converted the data into engineering units and performed the aircraft and engine performance calculations.

The resulting printout lists the identification for each channel and the engineering units used. As shown in this sample, 2215 digitized points resulted from the 27-second recording period. Using these data, the conversion program selected the highest and lowest values encountered during that period, calculated the mean value, the rms value, and the standard deviation, and printed out these values for each channel. The standard deviation was used to spot troublesome data channels.

Each of the PCM quantities used for the calculations on the last page of table C2 can be identified by using table C1. Table C3 lists by PCM identification code the formulas used to calculate the aircraft and engine performance parameters listed on the last page of the PCM listing (table C2).

TABLE C1.- TERMS FOR PCM DATA COMPUTATIONS FROM FLIGHT TEST

AB	absolute
ATIPREL	calculated relative angle of attack of air entering fan rotor at blade tip
AVE	average
BPF	blade-passage frequency for fan rotor (28 blades)
C	speed of sound
FPR	fan pressure ratio
HPT	blade-passage frequency for high-power turbine (71 blades)
IMP	blade-passage frequency for compressor rotor (16 blades)
IPAVE	average inlet static wall pressure calculated at inlet station 30.000
IP(X)AB	inlet static wall pressure measured at station 30.000 at circumferential location X (for $9 \leq X \leq 16$)
JT15D-1 once/rev	measured electronic signal which is a direct measurement of a single 360° rotation of fan rotor and which when averaged over time yields fan rotor rpm
LPT1	blade-passage frequency for first-stage low-power turbine (61 blades)
LPT2	blade-passage frequency for second-stage low-power turbine (55 blades)
MBP	calculated Mach number in the engine bypass duct at station 72.000
MFF	calculated Mach number at face of fan rotor
MINLET	calculated Mach number at station 30.000

TABLE C1.- Concluded

MTIP	calculated Mach number of rotor tip
MTIPREL	calculated relative Mach number of rotor tip
N1CORR	calculated corrected fan rotor rpm using JT15D-1 once/rev signal
P	pressure
PBPT	calculated average total pressure in the engine bypass at station 72.000
PDELAB	measured average absolute static pressure at location of bypass-duct total-pressure transducers, station 72.000
PDYNAM	dynamic pressure measurement from aircraft boom
PGRD	absolute ground pressure measurement recorded during preflight calibration
PSB	static pressure measurement from aircraft boom
PTOTAL	calculated total pressure
R(X)P(Y)AB	absolute total pressure measured at radial position (Y) by rake probes at circumferential location (X) in engine bypass duct (for $1 \leq Y \leq 6$ and $X = A, B, C$)
T	temperature
TI	temperature of air entering inlet
WCORR	calculated corrected total weight flow through engine
W30	calculated total weight flow through engine at station 30.000

TABLE C2.- PCM DATA LISTING

JT15D/DV1B FLIGHT TESTS KNIGHT/GOLUB JUNE 11,1981 RUN NO. 1043

FOR SERIAL NO. 4 THE START TIME IN HOURS,MINUTES, AND SECONDS IS 12 45 2.79 AND THE STOP TIME IS 12 45 29.99

CHANNEL	UNITS	HIGH	LOW	MEAN	RMS	STD	POINTS
TIME	SECONDS	45929.993	45902.786	45916.38949	45916.39016	7.85942	2215.
P-ATT	DEGREES	7.484	4.968	6.27892	6.30721	.59683	2215.
R-ATT	DEGREES	3.839	-2.484	.07706	1.74703	1.74573	2215.
ALPHA	DEGREES	10.594	3.725	7.38427	7.45088	.99426	2215.
BETA	DEGREES	2.769	-6.011	-1.96406	2.42487	1.42245	2215.
IP1	PSI	-.693	-.781	-.74330	.74340	.01226	2215.
IP2	PSI	-.651	-.741	-.70155	.70165	.01228	2215.
IP3	PSI	-.681	-.768	-.72994	.73004	.01250	2215.
IP4	PSI	-.696	-.795	-.74502	.74513	.01275	2215.
IP5	PSI	-.657	-.748	-.70392	.70403	.01248	2215.
IP6	PSI	-.555	-.658	-.61155	.61167	.01223	2215.
IP7	PSI	-.667	-.753	-.71979	.71990	.01249	2215.
IP8	PSI	-.683	-.775	-.73267	.73277	.01201	2215.
IP9	PSI	-.445	-.539	-.49480	.49497	.01311	2215.
IP10	PSI	-.449	-.536	-.50021	.50037	.01243	2215.
IP11	PSI	-.476	-.557	-.52686	.52699	.01187	2215.
IP12	PSI	-.485	-.572	-.53972	.53984	.01170	2215.
IP13	PSI	-.511	-.592	-.55955	.55968	.01165	2215.
IP14	PSI	-.518	-.600	-.56274	.56287	.01211	2215.
IP15	PSI	-.480	-.580	-.53055	.53071	.01301	2215.
IP16	PSI	-.447	-.546	-.49487	.49505	.01333	2215.
IP17	PSI	-.521	-.656	-.58763	.58801	.02111	2215.
IP18	PSI	-.618	-.719	-.67925	.67952	.01933	2215.
IP19	PSI	-.793	-.907	-.85802	.85819	.01711	2215.
IP20	PSI	-.670	-.831	-.74824	.74859	.02291	2215.
IP21	PSI	-.529	-.813	-.65783	.65949	.04674	2215.
IP22	PSI	-.381	-.544	-.46463	.46558	.02983	2215.
IP23	PSI	-.848	-1.101	-.98997	.99136	.05263	2215.
IP24	PSI	-.945	-1.207	-1.10257	1.10381	.05238	2215.
IP25	PSI	-1.142	-1.439	-1.32028	1.32116	.04817	2215.
IP26	PSI	-1.283	-1.583	-1.44765	1.44843	.04773	2215.
IP27	PSI	-1.225	-1.517	-1.37990	1.38089	.05231	2215.
IP28	PSI	-.983	-1.304	-1.13725	1.13863	.05600	2215.
IP29	PSI	-.960	-1.350	-1.18879	1.19055	.06487	2215.
IP30	PSI	-.299	-.773	-.57973	.58479	.07674	2215.
IP31	PSI	.287	.021	.14072	.14755	.04438	2215.
IP32	PSI	.411	.292	.35775	.35813	.01647	2215.
RAP1	PSI	4.036	3.783	3.92164	3.92185	.04043	2215.
RAP2	PSI	4.346	4.077	4.21607	4.21623	.03722	2215.
RAP3	PSI	4.333	4.142	4.23072	4.23082	.02809	2215.
RAP4	PSI	4.142	3.951	4.04827	4.04836	.02735	2215.
RAP5	PSI	4.020	3.843	3.94072	3.94081	.02620	2215.
RAP6	PSI	3.310	3.105	3.21257	3.21272	.03040	2215.
RBP1	PSI	4.172	3.640	3.91286	3.91372	.08172	2215.
RBP2	PSI	4.424	3.939	4.17433	4.17482	.06366	2215.
RBP3	PSI	4.306	3.817	4.11598	4.11642	.06025	2215.

TABLE C2.- Continued

RBP4	PSI	4.226	3.580	3.95022	3.95095	.07595	2215.
RBP5	PSI	3.985	3.251	3.67740	3.67940	.12124	2215.
RBP6	PSI	3.262	2.921	3.08582	3.08629	.05381	2215.
RCP1	PSI	4.097	3.518	3.78502	3.78608	.08980	2215.
RCP2	PSI	3.957	3.869	3.93005	3.93008	.01697	2215.
RCP3	PSI	4.297	3.917	4.11491	4.11534	.05991	2215.
RCP4	PSI	4.088	3.830	3.95568	3.95588	.03998	2215.
RCP5	PSI	4.043	3.766	3.91042	3.91063	.04059	2215.
RCP6	PSI	3.706	3.370	3.54672	3.54707	.04971	2215.
PDELTA	PSI	2.687	2.563	2.63425	2.63433	.01973	2215.
PDYNAM	PSI	.479	.386	.41323	.41346	.01363	2215.
PTOTAL	PSI	15.012	14.913	14.94235	14.94236	.01512	2215.
-PSB	PSI	-.111	-.128	-.11988	.11991	.00272	2215.
PENGAM	PSI	.031	-.095	-.02672	.03190	.01743	2215.
IP1AB	PSI	13.840	13.747	13.78582	13.78583	.01327	2215.
IP2AB	PSI	13.881	13.787	13.82758	13.82758	.01326	2215.
IP3AB	PSI	13.852	13.759	13.79918	13.79919	.01348	2215.
IP4AB	PSI	13.836	13.732	13.78410	13.78411	.01380	2215.
IP5AB	PSI	13.878	13.780	13.82520	13.82521	.01353	2215.
IP6AB	PSI	13.980	13.873	13.91757	13.91758	.01323	2215.
IP7AB	PSI	13.869	13.773	13.80933	13.80934	.01364	2215.
IP8AB	PSI	13.851	13.753	13.79645	13.79645	.01319	2215.
IP9AB	PSI	14.089	13.992	14.03432	14.03433	.01423	2215.
IP10AB	PSI	14.084	13.992	14.02891	14.02892	.01342	2215.
IP11AB	PSI	14.056	13.970	14.00226	14.00227	.01271	2215.
IP12AB	PSI	14.047	13.956	13.98941	13.98941	.01241	2215.
IP13AB	PSI	14.024	13.934	13.96957	13.96957	.01252	2215.
IP14AB	PSI	14.017	13.926	13.96638	13.96639	.01329	2215.
IP15AB	PSI	14.055	13.949	13.99858	13.99858	.01439	2215.
IP16AB	PSI	14.089	13.983	14.03425	14.03426	.01471	2215.
IP17AB	PSI	14.010	13.873	13.94149	13.94151	.02241	2215.
IP18AB	PSI	13.911	13.808	13.84987	13.84989	.01921	2215.
IP19AB	PSI	13.738	13.623	13.67110	13.67111	.01712	2215.
IP20AB	PSI	13.865	13.698	13.78088	13.78091	.02430	2215.
IP21AB	PSI	14.002	13.710	13.87129	13.87138	.04799	2215.
IP22AB	PSI	14.146	13.983	14.06449	14.06453	.02945	2215.
IP23AB	PSI	13.680	13.426	13.53916	13.53926	.05184	2215.
IP24AB	PSI	13.583	13.325	13.42656	13.42666	.05151	2215.
IP25AB	PSI	13.388	13.092	13.20884	13.20893	.04749	2215.
IP26AB	PSI	13.250	12.948	13.08148	13.08156	.04758	2215.
IP27AB	PSI	13.304	13.009	13.14922	13.14933	.05284	2215.
IP28AB	PSI	13.546	13.224	13.39187	13.39200	.05704	2215.
IP29AB	PSI	13.571	13.177	13.34034	13.34049	.06420	2215.
IP30AB	PSI	14.231	13.754	13.94939	13.94960	.07621	2215.
IP31AB	PSI	14.817	14.551	14.66984	14.66991	.04419	2215.
IP32AB	PSI	14.943	14.819	14.88687	14.88689	.01781	2215.
RAP1AB	PSI	18.569	18.311	18.45077	18.45081	.04048	2215.
RAP2AB	PSI	18.879	18.605	18.74519	18.74523	.03735	2215.
RAP3AB	PSI	18.868	18.666	18.75984	18.75987	.02864	2215.

TABLE C2.- Continued

RAP4AB	PSI	18.675	18.476	18.57739	18.57741	.02788	2215.
RAP5AB	PSI	18.555	18.374	18.46985	18.46987	.02642	2215.
RAP6AB	PSI	17.839	17.633	17.74169	17.74172	.03042	2215.
RBP1AB	PSI	18.705	18.170	18.44199	18.44217	.08191	2215.
RBP2AB	PSI	18.955	18.465	18.70345	18.70356	.06396	2215.
RBP3AB	PSI	18.837	18.346	18.64510	18.64520	.06054	2215.
RBP4AB	PSI	18.759	18.110	18.47934	18.47950	.07613	2215.
RBP5AB	PSI	18.516	17.782	18.20652	18.20693	.12132	2215.
RBP6AB	PSI	17.792	17.447	17.61494	17.61502	.05401	2215.
RCP1AB	PSI	18.630	18.053	18.31414	18.31436	.08988	2215.
RCP2AB	PSI	18.490	18.396	18.45917	18.45917	.01673	2215.
RCP3AB	PSI	18.822	18.447	18.64403	18.64413	.05991	2215.
RCP4AB	PSI	18.624	18.360	18.48480	18.48485	.04040	2215.
RCP5AB	PSI	18.573	18.296	18.43954	18.43959	.04084	2215.
RCP6AB	PSI	18.238	17.899	18.07584	18.07591	.05003	2215.
PDELAB	PSI	17.223	17.091	17.16338	17.16339	.02011	2215.
FF	PDS/HR	569.089	545.766	557.87494	557.88944	4.02371	2215.
RAT1	DEG F	121.404	118.748	120.20643	120.20693	.34798	2215.
RAT2	DEG F	118.748	116.535	117.52221	117.52273	.34900	2215.
RAT3	DEG F	115.650	113.437	114.47531	114.47586	.35489	2215.
RAT4	DEG F	114.322	112.109	113.17847	113.17903	.35673	2215.
RAT5	DEG F	117.863	115.650	116.49512	116.49558	.32612	2215.
RBT1	DEG F	120.519	118.306	119.52264	119.52312	.34194	2215.
RBT2	DEG F	117.420	114.765	116.11326	116.11384	.36687	2215.
RBT3	DEG F	116.092	113.437	114.59581	114.59638	.36147	2215.
RBT4	DEG F	116.535	113.879	115.17709	115.17761	.34571	2215.
RBT5	DEG F	119.191	-178.595	105.08005	120.97826	59.96286	2215.
RCT1	DEG F	120.076	117.863	118.97132	118.97183	.34788	2215.
RCT2	DEG F	117.420	115.207	116.26672	116.26726	.35405	2215.
RCT3	DEG F	114.765	112.552	113.80631	113.80683	.34324	2215.
RCT4	DEG F	113.879	112.109	112.87473	112.87526	.34466	2215.
RCT5	DEG F	114.765	112.552	113.48160	113.48213	.34885	2215.
TF	DEG F	93.520	91.749	92.68825	92.68880	.31859	2215.
TI	DEG F	73.602	71.389	72.71857	72.71939	.34587	2215.
TENGAM	DEG F	108.126	105.913	106.97217	106.97269	.33243	2215.
TAIR-S	DEG F	75.815	73.160	74.80752	74.80842	.36690	2215.
TALT-S	DEG F	77.586	75.815	76.45845	76.45903	.29849	2215.
TRMDV	DEG F	91.749	89.536	90.81052	90.81099	.29279	2215.
ITT	DEG F	1026.223	1013.052	1019.46038	1019.46263	2.14108	2215.
TTOTAL	DEG F	78.540	73.340	75.53104	75.53294	.53568	2215.
T53-N1	RPM	22031.239	21243.047	21641.04397	21641.37655	120.00698	2215.
T53-N2	RPM	1611.679	1555.926	1585.39081	1585.42032	9.67534	2215.
JT15-N1	RPM	11971.534	11859.008	11919.81154	11919.82044	14.57123	2215.
JT15-N2	RPM	27100.058	27037.435	27065.99478	27065.99752	12.16929	2215.
JT15-1/REV	RPM	11952.191	11881.188	11912.83272	11912.83978	12.97151	2215.
JT15-FFREQ	RPS	666.667	617.284	639.06314	639.10174	7.02578	2215.

TABLE C2.- Concluded

SPEED OF SOUND IN INLET(FPS)	C =	1131.3279
MACH NUMBERS	MINLET =	.3060
	MFF =	.3360
	MTIP =	.9645
	MTIPREL =	1.0214
	MBP =	.3316
	MAC =	.2006
TIP RELATIVE FLOW ANGLE(DEG)	ATIPREL =	1.1984
INLET PRESSURES(PSI)	IPAVE =	14.0030
	PTOTAL =	14.9424
BYPASS PRESSURES(PSI)	PDELAB =	17.1634
	PBPT =	18.5214
FAN PRESSURE RATIO	FPR =	1.2395
INLET WEIGHT FLOWS(LBS/SEC)	W30 =	55.4938
	WCORR =	55.2960
ROTATIONAL SPEEDS(RPM)	JT15-1/REV =	11912.8327
	N1CORR =	11758.3551
	JT15-N2 =	27065.9948
ACOUSTIC FREQUENCIES(HZ)	BPF =	5559.7190
	IMP =	7218.5008
	HPT =	32027.1916
	LPT1 =	12111.7770
	LPT2 =	10920.4938

THE NUMBER OF FRAMES IN SERIAL 4 = 2215

TABLE C3.- COMPUTATIONS USING PCM DATA

$$C = 49.03\sqrt{TI + 459.7}$$

$$IPAVE = \frac{IP9AB + IP10AB + IP11AB + IP12AB + IP13AB + IP14AB + IP15AB + IP16AB}{8}$$

$$PTOTAL = PDYNAM + (-PSB) + PGRD$$

$$\begin{aligned} PBPT = \frac{1}{15}(&RAP1AB + RAP2AB + RAP3AB + RAP4AB + RAP5AB \\ &+ RBP1AB + RBP2AB + RBP3AB + RBP4AB + RBP5AB \\ &+ RCP1AB + RCP2AB + RCP3AB + RCP4AB + RCP5AB) \end{aligned}$$

$$MINLET = \left\{5\left[\left(\frac{PTOTAL}{IPAVE}\right)^{0.2857} - 1\right]\right\}^{0.5000}$$

$$MTIP = 0.0916 \times (\text{JT15D-1 once per rev})/C$$

$$MFF = 1.098 \times MINLET$$

$$MTIPREL = \sqrt{(MFF)^2 + (MTIP)^2}$$

$$MBP = \left\{5\left[\left(\frac{PBPT}{PDELAB}\right)^{0.2857} - 1\right]\right\}^{0.5000}$$

TABLE C3.- Concluded

ATIPREL = 72° - arctan(MTIP/MFF)

$$W30 = 296.1\left(\frac{PTOTAL}{\sqrt{TI + 459.7}}\right)\left\{\frac{MINLET}{[1 + 0.2(MINLET)^2]^3}\right\}$$

$$WCORR = W30\sqrt{\left(\frac{TI + 459.7}{518.7}\right)\left(\frac{14.696}{PTOTAL}\right)} = \left\{\frac{MINLET}{[1 + 0.2(MINLET)^2]^3}\right\}191.06425$$

$$FPR = \frac{PBPT}{PTOTAL}$$

$$N1CORR = \text{JT15D-1 once per rev}\Big/\sqrt{\frac{TI + 459.7}{518.7}}$$

BPF = 0.4667 × (JT15D-1 once/rev)

IMP = 0.2667 × JT15D-1 N2 speed

HPT = 1.1833 × JT15D-1 N2 speed

LPT1 = 1.0167 × JT15D-1 once/rev

LPT2 = 0.9167 × JT15D-1 once/rev

REFERENCES

1. Feiler, Charles E.; and Merriman, James E.: Effects of Forward Velocity and Acoustic Treatment on Inlet Fan Noise. AIAA Paper 74-946, Aug. 1974.

2. Tyler, J. M.; and Sofrin, T. G.: Axial Flow Compressor Noise Studies. SAE Trans., vol. 70, 1962, pp. 309-332.

3. Hanson, Donald B.: Spectrum of Rotor Noise Caused by Atmospheric Turbulence. J. Acoust. Soc. America, vol. 56, no. 1, July 1974, pp. 110-126.

4. Feiler, Charles E.; and Groeneweg, John F.: Summary of Forward Velocity Effects on Fan Noise. NASA TM-73722, 1977.

5. Sloan, Denis; Farquhar, Bannister W.; and Rayl, Christopher: The Influence of the Inlet Duct Contour on Forward Radiated Fan Noise. AIAA Paper 77-1355, Oct. 1977.

6. Preisser, John S.; and Chestnutt, David: Flight Effects on Fan Noise With Static and Wind Tunnel Comparisons. AIAA-83-0678, Apr. 1983.

7. Schoenster, James A.: Fluctuating Pressure Measurements on the Fan Blades of a Turbofan Engine During Ground and Flight Tests. AIAA-83-0679, Apr. 1983.

8. Mueller, Arnold W.: Study of Stator-Vane Fluctuating Pressures in a Turbofan Engine for Static and Flight Tests. NASA TP-2217, 1984.

9. Chestnutt, David, ed.: Flight Effects of Fan Noise. NASA CP-2242, 1982.

10. Mueller, Arnold W.; and Preisser, John S.: Flight Test of a Pure-Tone Acoustic Source. NASA TP-1898, 1981.

11. Gridley, Doreen: Program for Narrow-Band Analysis of Aircraft Flyover Noise Using Ensemble Averaging Techniques. NASA CR-165867, 1982.

12. Instrumentation Handbook - Volume I. Radar Facilities and Systems, Wallops Flight Center, May 1976.

13. Hodder, Brent K.: An Investigation of Possible Causes for the Reduction of Fan Noise in Flight. AIAA Paper No. 76-585, July 1976.

14. Hodder, Brent K.: Further Studies of Static to Flight Effects on Fan Tone Noise Using Inlet Distortion Control for Source Identification. NASA TM X-73183, 1976.

15. Plucinsky, J. C.: 'Quiet' Aspects of the Pratt and Whitney Aircraft JT15D Turbofan. SAE Paper 730289, Apr. 1973.

16. Peracchio, A. A.; Ganz, U. W.; Gedge, M.; and Robbins, K.: Studies on Proper Simulation During Static Testing of Forward Speed Effects on Fan Noise. NASA CR-165626, 1980.

17. Grumman Aerospace Corporation: Final Report of the Feasibility Study for the Installation and Test of a Pratt and Whitney Turbofan Engine on a Mohawk Aircraft. NASA CR-145314, 1978.

18. Knight, Vernie H., Jr.: In-Flight Jet Engine Noise Measurement System. Instrumentation in the Aerospace Industry - Volume 27, Advances in Test Measurement - Volume 18, Part One, Proceedings of the 27th International Instrumentation Symposium, Instrum. Soc. America, 1981, pp. 381-386.

19. Preisser, J. S.; Schoenster, J. A.; Golub, R. A.; and Horne, C.: Unsteady Fan Blade Pressure and Acoustic Radiation From a JT15D-1 Turbofan Engine at Simulated Forward Speed. AIAA-81-0096, Jan. 1981.

20. Falarski, Michael D.; and Moore, Michael T.: Acoustic Characteristics of Two Hybrid Inlets at Forward Speed. J. Aircr., vol. 17, no. 2, Feb. 1980, pp. 106-111.

21. Jones, W. L.; McArdle, J. G.; and Homyak, L.: Evaluation of Two Inflow Control Devices for Flight Simulation of Fan Noise Using a JT15D Engine. AIAA Paper 79-0654, Mar. 1979.

22. McArdle, J. G.; Jones, W. L.; Heidelberg, L. J.; and Homyak, L.: Comparison of Several Inflow Control Devices for Flight Simulation of Fan Tone Noise Using a JT15D-1 Engine. NASA TM-81505, 1980.

23. Homyak, L.; McArdle, J. G.; and Heidelberg, L. J.: A Compact Inflow Control Device for Simulating Flight Fan Noise. AIAA-83-0680, Apr. 1982.

24. Stockman, Norbert O.; and Farrell, Charles A., Jr.: Improved Computer Programs for Calculating Potential Flow in Propulsion System Inlets. NASA TM-73728, 1977.

25. Holm, R. G.; Langenbrunner, L. E.; and McCann, E. O.: Forward Velocity Effects on Fan Noise and the Influence of Inlet Aeroacoustic Design as Measured in the NASA-Ames 40 × 80 Foot Wind Tunnel. NASA CR-152329, 1981.

26. Ginder, R. B.; and Newby, D. R.: An Improved Correlation for the Broadband Noise of High-Speed Fans. J. Aircr., vol. 14, no. 9, Sept. 1977, pp. 844-849.

27. Sines, G.: Final Report for NASA/JT15D Engine Installation on OV-1B Mohawk Aircraft 62-5880. NASA CR-159299, 1980.

28. Schoenster, James A.: Fluctuating Pressures on Fan Blades of a Turbofan Engine - Static and Wind-Tunnel Investigations. NASA TP-1976, 1982.

1. Report No. NASA TP-2254	2. Government Accession No.	3. Recipient's Catalog No.
4. Title and Subtitle TEST-ENGINE AND INLET PERFORMANCE OF AN AIRCRAFT USED FOR INVESTIGATING FLIGHT EFFECTS ON FAN NOISE		5. Report Date April 1984
		6. Performing Organization Code 505-31-33-13
7. Author(s) Robert A. Golub and John S. Preisser		8. Performing Organization Report No. L-15653
9. Performing Organization Name and Address NASA Langley Research Center Hampton, VA 23665		10. Work Unit No.
		11. Contract or Grant No.
12. Sponsoring Agency Name and Address National Aeronautics and Space Administration Washington, DC 20546		13. Type of Report and Period Covered Technical Paper
		14. Sponsoring Agency Code

15. Supplementary Notes

16. Abstract

As part of the NASA Flight Effects on Fan Noise Program, a Grumman OV-1B Mohawk aircraft was modified to carry a modified and instrumented Pratt & Whitney JT15D-1 turbofan engine. Onboard flight data, together with simultaneously measured far-field acoustic data, comprise a flight data base to which JT15D-1 static and wind-tunnel data are compared. The overall objective is to improve the ability to use ground-based facilities for the prediction of flight inlet radiated noise. This report describes the hardware and presents performance results for the research engine.

17. Key Words (Suggested by Author(s)) Fan noise Flight effects Turbofan engine	18. Distribution Statement Unclassified - Unlimited Subject Category 71

19. Security Classif. (of this report)	20. Security Classif. (of this page)	21. No. of Pages	22. Price
Unclassified	Unclassified	68	A04

For sale by the National Technical Information Service, Springfield, Virginia 22161 NASA-Langley, 1984

National Aeronautics and
Space Administration

Washington, D.C.
20546

Official Business
Penalty for Private Use, $300

THIRD-CLASS BULK RATE

Postage and Fees Paid
National Aeronautics and
Space Administration
NASA-451

U.S.MAIL

1 1 1U,H, 840328 S00903DS
DEPT OF THE AIR FORCE
AF WEAPONS LABORATORY
ATTN: TECHNICAL LIBRARY (SUL)
KIRTLAND AFB NM 87116

S

NASA

POSTMASTER: If Undeliverable (Section 158
Postal Manual) Do Not Return